J. Fluid Mech. (2010), *vol.* 665, *pp.* 238–273.
doi:10.1017/S0022112010003927

Large-eddy simulation of the compressible flow past a wavy cylinder

CHANG-YUE XU, LI-WEI CHEN AND XI-YUN LU†

Department of Modern Mechanics, University of Science and Technology of China, Hefei, Anhui 230026, China

(Received 8 January 2010; revised 18 July 2010; accepted 19 July 2010; first published online 22 October 2010)

Numerical investigation of the compressible flow past a wavy cylinder was carried out using large-eddy simulation for a free-stream Mach number $M_\infty = 0.75$ and a Reynolds number based on the mean diameter $Re = 2 \times 10^5$. The flow past a corresponding circular cylinder was also calculated for comparison and validation against experimental data. Various fundamental mechanisms dictating the intricate flow phenomena, including drag reduction and fluctuating force suppression, shock and shocklet elimination, and three-dimensional separation and separated shear-layer instability, have been studied systematically. Because of the passive control of the flow over a wavy cylinder, the mean drag coefficient of the wavy cylinder is less than that of the circular cylinder with a drag reduction up to 26 %, and the fluctuating force coefficients are significantly suppressed to be nearly zero. The vortical structures near the base region of the wavy cylinder are much less vigorous than those of the circular cylinder. The three-dimensional shear-layer shed from the wavy cylinder is more stable than that from the circular cylinder. The vortex roll up of the shear layer from the wavy cylinder is delayed to a further downstream location, leading to a higher-base-pressure distribution. The spanwise pressure gradient and the baroclinic effect play an important role in generating an oblique vortical perturbation at the separated shear layer, which may moderate the increase of the fluctuations at the shear layer and reduce the growth rate of the shear layer. The analysis of the convective Mach number indicates that the instability processes in the shear-layer evolution are derived from oblique modes and bi-dimensional instability modes and their competition. The two-layer structures of the shear layer are captured using the instantaneous Lamb vector divergence, and the underlying dynamical processes associated with the drag reduction are clarified. Moreover, some phenomena relevant to the compressible effect, such as shock waves, shocklets and shock/turbulence interaction, are analysed. It is found that the shocks and shocklets which exist in the circular cylinder flow are eliminated for the wavy cylinder flow and the wavy surface provides an effective way of shock control. As the shock/turbulence interaction is avoided, a significant drop of the turbulent fluctuations around the wavy cylinder occurs. The results obtained in this study provide physical insight into the understanding of the mechanisms relevant to the passive control of the compressible flow past a wavy surface.

Key words: compressible turbulence, drag reduction, turbulence simulation

† Email address for correspondence: xlu@ustc.edu.cn

1. Introduction

Owing to the obvious importance in a wide range of fundamental studies and applications, a significant effort has been made in recent decades to study the control of flow over a bluff body, typically a canonical geometry circular cylinder. Comprehensive reviews on this subject have been given in the literature (e.g. Oertel & Affiliation 1990; Williamson & Govardhan 2004; Choi, Jeon & Kim 2008), where significant progress has been achieved for the incompressible flow past a bluff body. Moreover, the control of the compressible flow in the transonic regime over a bluff body is responsible for some important issues related to the coupled shearing and compressing processes, such as compressible turbulent flow-separation control, shock control, shock/turbulence interaction and acoustics (e.g. Peake & Crighton 2000; Stanewsky 2001; Bushnell 2004). However, the physical mechanisms dictating the characteristics of compressible flow control are still unclear and are of great interest for further detailed studies.

Extensive work has been conducted on the control of flow over a bluff body in recent decades. Recently, Choi *et al.* (2008) classified control methods for bluff-body flows as boundary-layer controls and direct-wake modifications, depending on whether the control delays separation by modifying the boundary layer or changes directly the wake characteristics. In direct-wake-control methods, two groups were classified in terms of two-dimensional (2D) or three-dimensional (3D) disturbances in the spanwise direction of a bluff body (Choi *et al.* 2008). One group was called '2D forcing', such as the disturbances with a splitter plate (Anderson & Szewczyk 1997; Ozono 1999; Hwang, Yang & Sun 2003), tabs (Thombi, Daisuke & Yoshiaki 2002) and base bleed (Delaunay & Kaiktsis 2001; Yao & Sandham 2002; Arcas & Redekopp 2004). The other group was named '3D forcing', such as the disturbances with a wavy trailing edge (Thombazis & Bearman 1997; Cai, Chng & Tsai 2008) and a wavy surface of cylinder (e.g. Lee & Nguyen 2007; Lam & Lin 2008, 2009).

Using the '3D forcing' direct-wake control, some work has been performed for flow over a wavy cylinder whose diameter varied sinusoidally along its spanwise direction. Ahmed & Bays-Muchmore (1992) and Ahmed, Khan & Bays-Muchmore (1993) investigated experimentally the pressure field and flow patterns over a wavy cylinder. Lam *et al.* (2004*a*) and Lam, Wang & So (2004*b*) performed experiments to deal with the drag reduction and the relevant flow-induced vibration for different wavy cylinders. Zhang, Dai & Lee (2005) used the particle-image-velocimetry technique to investigate the flow structures in the near wake of a wavy cylinder and demonstrated well-organized streamwise vortices in the spanwise direction. Lee & Nguyen (2007) measured the forces on wavy cylinders with different geometric parameters and found the maximum drag reduction of up to 22 % relative to the corresponding circular cylinder. Recently, Lam & Lin (2008, 2009) also studied numerically the turbulent and laminar flow over wavy cylinders. These studies revealed that the wavy surface can lead to the formation of a 3D shear layer, which is more stable than the 2D shear layer. Moreover, we need to indicate that all these previous investigations are only to deal with the incompressible flow over a wavy cylinder. To our knowledge, however, the relevant study for the compressible flow past a wavy cylinder has never been performed.

Initially, the compressible flow in the transonic regime over a circular cylinder, which is a prototype of a wavy cylinder, is introduced in order to understand its underlying complex flow phenomena, such as shock/turbulent-boundary-layer interaction, shock/wake interaction and compressible boundary layer instability. Experiments on the transonic flow past a circular cylinder have been performed by Macha (1977), Murthy & Rose (1978) and Rodriguez (1984) for the Reynolds number about 10^5.

They mainly focused on the drag-force measurements and flow visualizations. Murthy & Rose (1978) used buried wire gauges to measure skin friction and vortex-shedding frequency. Moreover, the 2D compressible Navier–Stokes equations were numerically solved using a finite-volume method to investigate the unsteady forces and flow structures for transonic flow past a circular cylinder (Miserda & Leal 2006). Recently, the effect of Mach number on transonic flow past a circular cylinder has been studied numerically (Xu, Chen & Lu 2009*a*). They mainly discussed several salient features, including shock/turbulent-boundary-layer interaction, formation of a local supersonic zone (LSZ) and shocklet in the wake, and evolution of a turbulent shear layer. Thus, compared with the incompressible flow control, an effective control of the compressible flow past a bluff body is responsible for additional flow features relevant to the compressible effect, such as shock wave and shock/turbulence interaction.

The development of a 3D free-shear-layer shed from a wavy cylinder plays an important role in the drag reduction and fluctuating lift suppression (e.g. Lam & Lin 2008, 2009). For the compressible flow past the cylinder, the shearing and compressing processes should be coupled to affect the shear-layer evolution. A direct effect of the compressibility is related to the convective Mach number, M_c (Bogdanoff 1983; Papamoschou & Roshko 1988). According to experiments (e.g. Gruber, Messersmith & Dutton 1993; Barre, Quine & Dussauge 1994; Clemens & Mungal 1995) and direct numerical simulations (e.g. Sandham & Reynolds 1991; Sarkar 1995; Vreman, Sandham & Luo 1996; Pantano & Sarkar 2002), it was found that the normalized pressure–strain term decreases with increasing M_c and the consequence of the compressibility effect involves a decay of the turbulence production term in the Reynolds-stresses transport equation. Moreover, when $M_c < 0.6$, the instability process is bi-dimensional with spanwise correlated structures originating from the Kelvin–Helmholtz instability. When $0.6 < M_c < 1$, oblique wave modes compete with bi-dimensional instability modes. Further, when $M_c > 1$, the instability waves are 3D and the growth rate of the most amplified mode is greatly reduced (Simon *et al.* 2007). The separation process over a wavy cylinder will generate a 3D compressible shear layer, leading to the occurrence of instability modes coupled with complex interactions. This particular geometrical configuration results in a significant modification of the whole flow field compared with the circular cylinder case, which may be associated with some features of the compressible flow control that need to be studied.

The turbulent-boundary-layer separation and the relevant vortical structures of a bluff cylinder play an important role in overall flow behaviours. Characterizing dynamical processes in flow evolution is still one of the fundamental challenges in fluid mechanics. Usually, the dynamical processes are analysed by the proper orthogonal decomposition (Lumley 1967; Berkooz, Holmes & Lumley 1993) and stochastic estimation (Adrian & Moin 1988) methods, and vortical structures are often discussed relative to the importance of vortices (e.g. Robinson 1991; Jeong & Hussain 1995; Chakraborty, Balachandar & Adrian 2005). Moreover, the Lamb vector acts as a vortex force and its character plays an important role in establishing the nature of the flow (Truesdell 1954; Wu, Lu & Zhuang 2007). The Lamb vector divergence is associated with the momentum transport in the flow field (Wu *et al.* 2007) and appears as an acoustic source term in Lighthill's wave equation (Lighthill 1952; Howe 1975). Recently, the mathematical properties and physical interpretations of the Lamb vector divergence that substantiate its kinematical and dynamical significance have been analysed by Hamman, Klewicki & Kirby (2008). They found that the

Lamb vector divergence may provide a rigorous methodology for the study of what are generically referred to as coherent structures or motions. The distribution of the Lamb vector divergence is also related to the forces on a body and can be used to clarify the underlying dynamical processes which are associated with the drag reduction.

In this paper, a large-eddy simulation (LES) technique, which has provided a powerful tool for studying the dynamics of turbulent flows, is utilized to investigate the compressible flow past a wavy cylinder and a corresponding circular cylinder. The purpose is to achieve an improved understanding of some of the fundamental phenomena in this flow, including drag reduction and fluctuating force suppression, shock and shocklet elimination, 3D separation and separated shear-layer instability and flow structures. Special attention is given to the effects of the wavy surface on the features of the compressible flow control.

This paper is organized as follows. The mathematical formulation and numerical methods are presented in § 2. The computational overview and validation are described in § 3. Detailed results are then given in § 4 and the concluding remarks in § 5.

2. Mathematical formulation and numerical methods

2.1. *Filtered governing equations*

Large-eddy simulations are implemented in this study for turbulence closure, in which large-scale motions are explicitly computed and eddies with scales smaller than the grid or filter size are modelled to represent the effects of unresolved motions on resolved scales. The 3D Favre-filtered conservation equations of mass, momentum and energy are employed. To non-dimensionalize the equations, we use the free-stream variables including the density, ρ_∞, temperature, T_∞, free-stream velocity, U_∞, and the mean diameter of the wavy cylinder as characteristic quantities. Then, the non-dimensional equations can be expressed as (Lu *et al.* 2005)

$$\frac{\partial \bar{\rho}}{\partial t} + \frac{\partial (\bar{\rho}\tilde{u}_i)}{\partial x_i} = 0, \tag{2.1}$$

$$\frac{\partial \bar{\rho}\tilde{u}_i}{\partial t} + \frac{\partial (\bar{\rho}\tilde{u}_i\tilde{u}_j)}{\partial x_j} = -\frac{\partial \bar{p}}{\partial x_i} + \frac{\partial \left(\tilde{\tau}_{ij} - \tau_{ij}^{SGS} + D_{ij}^{SGS}\right)}{\partial x_j}, \tag{2.2}$$

$$\frac{\partial \bar{\rho}\tilde{E}}{\partial t} + \frac{\partial [(\bar{\rho}\tilde{E} + \bar{p})\tilde{u}_i]}{\partial x_i} = \frac{\partial}{\partial x_i}\left(-\tilde{q}_i + \tilde{u}_j\tilde{\tau}_{ij} + \mathscr{J}_i^{SGS} + \sigma_i^{SGS} - Q_i^{SGS} - H_i^{SGS}\right), \tag{2.3}$$

where an overbar denotes the spatial filter and a tilde the Favre filter, i.e. $\tilde{f} = \overline{\rho f}/\bar{\rho}$. The variables ρ, u_i, p and E represent the density, velocity component, pressure and specific total energy, respectively. The diffusive fluxes are given by

$$\tilde{\tau}_{ij} = 2\tilde{\mu}\tilde{S}_{ij} - \tfrac{2}{3}\tilde{\mu}\delta_{ij}\tilde{S}_{kk}, \tag{2.4}$$

$$\tilde{q}_i = -\frac{\tilde{\mu}C_p}{Pr}\frac{\partial \tilde{T}}{\partial x_i}, \tag{2.5}$$

where μ is the molecular viscosity, C_p is the constant-pressure specific heat, Pr is the Prandtl number and S_{ij} represents the strain-rate tensor defined as $S_{ij} = (\partial u_i/\partial x_j + \partial u_j/\partial x_i)/2$. The perfect gas relationship and the Sutherland law for the molecular viscosity coefficient, μ, are employed.

The subgrid closure terms in (2.2) and (2.3) are defined as

$$\tau_{ij}^{SGS} = \bar{\rho}(\widetilde{u_i u_j} - \tilde{u}_i \tilde{u}_j), \tag{2.6}$$

$$D_{ij}^{SGS} = (\bar{\tau}_{ij} - \tilde{\tau}_{ij}), \tag{2.7}$$

$$\mathscr{J}_i^{SGS} = -\tfrac{1}{2}\bar{\rho}(u_i\widetilde{u_k u_k} - \tilde{u}_i\widetilde{u_k u_k}), \tag{2.8}$$

$$Q_i^{SGS} = (\bar{q}_i - \tilde{q}_i), \tag{2.9}$$

$$H_i^{SGS} = C_p(\widetilde{\bar{\rho} u_i T} - \bar{\rho}\tilde{u}_i \tilde{T}), \tag{2.10}$$

$$\sigma_i^{SGS} = (\widetilde{u_j \tau_{ij}} - \tilde{u}_j \tilde{\tau}_{ij}). \tag{2.11}$$

These terms arise from the unresolved scales and need to be modelled in terms of the resolved scales. Because the filter scale of LES falls in the inertial subrange of the turbulent-kinetic-energy (TKE) spectrum, the modelling of subgrid terms is relatively universal in comparison with that of the simulation of the Reynolds-averaged Navier–Stokes equations.

2.2. *Subgrid-scale models*

The introduction of the dynamic model proposed by Germano *et al.* (1991) has spurred significant progress in the subgrid-scale (SGS) modelling of non-equilibrium flows. Among the various SGS turbulence models, such as the mixed model (Fureby 1996) and the two-parameter mixed model (Salvetti & Banerjee 1995), the dynamic SGS model for turbulence closure offers the best trade-off between accuracy and cost (Desjardin & Frankel 1998). In the present study, the dynamic Smagorinsky model for compressible flows proposed by Moin *et al.* (1991) is employed. The anisotropic part of the SGS stresses (2.6) is treated by using the Smagorinsky model (Smagorinsky 1963), while the isotropic part τ_{kk}^{SGS} is modelled with a formulation proposed by Yoshizawa (1986)

$$\tau_{ij}^{SGS} - \tfrac{1}{3}\delta_{ij}\tau_{kk}^{SGS} = -2C_R\bar{\Delta}^2\bar{\rho}|\tilde{S}|\left(\tilde{S}_{ij} - \tfrac{1}{3}\delta_{ij}\tilde{S}_{kk}\right) = C_R\alpha_{ij}, \tag{2.12}$$

$$\tau_{kk}^{SGS} = 2C_I\bar{\Delta}^2\bar{\rho}|\tilde{S}|^2 = C_I\alpha, \tag{2.13}$$

where $\alpha_{ij} = -2\bar{\Delta}^2\bar{\rho}|\tilde{S}|(\tilde{S}_{ij} - (1/3)\delta_{ij}\tilde{S}_{kk})$, $\alpha = 2\bar{\Delta}^2\bar{\rho}|\tilde{S}|^2$ and $|\tilde{S}| = (2\tilde{S}_{ij}\tilde{S}_{ij})^{1/2}$. C_R and C_I are the model coefficients and are determined dynamically during the calculation. The model utilizes the information about resolved scales at the grid-filter level and at a coarser test-filter level with $\hat{\Delta} > \bar{\Delta}$. The least-squares method proposed by Lilly (1992) is then implemented to obtain the two coefficients

$$C_R = \frac{\langle L_{ij}M_{ij}\rangle}{\langle M_{kl}M_{kl}\rangle} - \frac{1}{3}\frac{\langle L_{mm}M_{nn}\rangle}{\langle M_{kl}M_{kl}\rangle}, \tag{2.14}$$

$$C_I = \frac{\langle L_{kk}\rangle}{\langle \beta - \hat{\alpha}\rangle}. \tag{2.15}$$

The brackets $\langle\cdot\rangle$ denote local smoothing, which is used to circumvent the numerical instability originating from the dynamic calculation of the eddy-viscosity model coefficients (Germano *et al.* 1991; Moin *et al.* 1991). A local volume-weighted average with around 27 points is employed for the local smoothing (Fureby 1996; Desjardin & Frankel 1998). Additional clipping based on the entropy-limit condition of the form $\mu + \mu_T \geqslant 0$ is implemented to limit the extent of backscattering in the calculation (e.g. Lu *et al.* 2005), where μ_T is the SGS turbulent viscosity. In the present study, the fraction of grid points requiring additional clipping is less than 1 %. The forms

of L_{ij}, M_{ij} and β are

$$L_{ij} = \widehat{\bar{\rho}\tilde{u}_i\tilde{u}_j} - \hat{\bar{\rho}}\tilde{\tilde{u}}_i\tilde{\tilde{u}}_j, \tag{2.16}$$

$$M_{ij} = \beta_{ij} - \hat{\alpha}_{ij}; \quad \beta_{ij} = -2\hat{\Delta}^2\hat{\bar{\rho}}|\tilde{\tilde{S}}|\left(\tilde{\tilde{S}}_{ij} - \tfrac{1}{3}\delta_{ij}\tilde{\tilde{S}}_{kk}\right); \quad \beta = 2\hat{\Delta}^2\hat{\bar{\rho}}|\tilde{\tilde{S}}|^2, \tag{2.17}$$

where the hat represents the test-filtered variable. A Favre-filtered variable at the test-filter level is defined as $\tilde{\tilde{f}} = \widehat{\bar{\rho}f}/\hat{\bar{\rho}}$.

The subgrid energy flux term is

$$H_i^{SGS} = C_p(\widetilde{\bar{\rho}u_iT} - \bar{\rho}\tilde{u}_i\tilde{T}) = -\frac{\mu_t C_p}{Pr_t}\frac{\partial\tilde{T}}{\partial x_j}, \tag{2.18}$$

where $\mu_t = \bar{\rho}C_R\bar{\Delta}^2|\tilde{S}|$. Similarly, the turbulent Prandtl number Pr_t is determined as

$$Pr_t = \frac{C_R\langle K_jK_j\rangle}{\langle N_iK_i\rangle}, \tag{2.19}$$

where

$$N_i = \widehat{\bar{\rho}\tilde{u}_i\tilde{T}} - \hat{\bar{\rho}}\tilde{\tilde{u}}_i\tilde{\tilde{T}}; \quad K_i = \bar{\Delta}^2\bar{\rho}\left|\widehat{\tilde{S}\frac{\partial\tilde{T}}{\partial x_i}}\right| - \hat{\Delta}^2\hat{\bar{\rho}}|\tilde{\tilde{S}}|\frac{\partial\tilde{\tilde{T}}}{\partial x_i}. \tag{2.20}$$

The SGS turbulent diffusion term is reasonably modelled as $\mathscr{J}_i^{SGS} = \tilde{u}_j\tau_{ij}^{SGS}$ (Knight *et al.* 1998). The treatments of the viscous stress term, D_{ij}^{SGS}, and the heat flux term, Q_i^{SGS}, have been analysed by Piomelli (1999). The SGS viscous diffusion term σ_i^{SGS} is neglected because of its small contribution in the energy equation (Martin, Piomelli & Candler 1999).

2.3. *Numerical procedure*

The governing equations are numerically solved by a finite-volume method. The convective terms are discretized by a second-order central/upwind hybrid scheme for shock-capturing and the viscous terms by a fourth-order central difference (Lu *et al.* 2005; Wang *et al.* 2007; Chen, Xu & Lu 2010*a*). The temporal integration is performed using an implicit approximate-factorization method with sub-iterations to ensure the second-order accuracy (Simon *et al.* 2007).

To capture the discontinuity caused by a shock wave, a second-order upwind scheme with the Roe's flux-difference splitting is introduced into the inviscid flux. The spatial discretization has been constructed explicitly to be shock capturing with the upwind scheme and to revert to a central stencil with low numerical dissipation in turbulent flow regions away from shock. A binary sensor function $\Phi_{i+1/2}$ at cell face $i+1/2$ is used for the detection of shocks; $\Phi_{i+1/2}$ is determined by the pressure and density curvature criteria proposed by Hill, Pantano & Pullin (2006)

$$\alpha_p^{i+1/2} = \max\left(\alpha_p^i, \alpha_p^{i+1}\right), \quad \alpha_\rho^{i+1/2} = \max\left(\alpha_\rho^i, \alpha_\rho^{i+1}\right) \tag{2.21}$$

and

$$\alpha_p^i = \left|\frac{p_{i+1} - 2p_i + p_{i-1}}{p_{i+1} + 2p_i + p_{i-1}}\right|, \quad \alpha_\rho^i = \left|\frac{\rho_{i+1} - 2\rho_i + \rho_{i-1}}{\rho_{i+1} + 2\rho_i + \rho_{i-1}}\right|, \tag{2.22}$$

where α_p^i and α_ρ^i represent the pressure and density relative curvatures at the cell centre, respectively. When $\alpha_p^{i+1/2} > c_1$ and $\alpha_\rho^{i+1/2} > c_2$, $\Phi_{i+1/2}$ is 1; but zero, otherwise. The 3D version of this detection is used in the simulations. Similar to the treatment (Hill *et al.* 2006), the values of c_1 and c_2 that proved to give the best results are

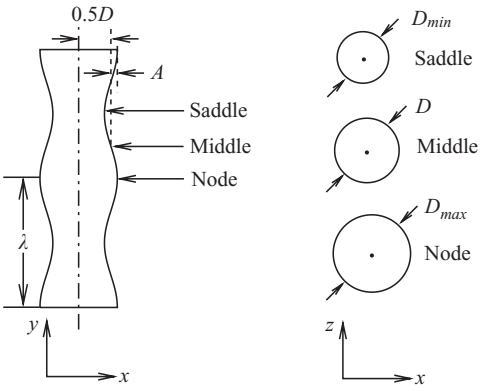

FIGURE 1. Schematic diagram of a wavy cylinder.

chosen as 0.01 (Chen *et al.* 2010*a*). Based on this detection, the Roe's second-order upwind flux only operates at the cells in the vicinity of a shock wave.

To assess the use of the numerical schemes for LES of turbulent flow, the instantaneous region of upwind flux was examined and the fraction of grid points occupied by the upwind flux is much less than 1 % during the calculations. Moreover, an analysis of the SGS and numerical kinetic energy dissipation has been performed by Ducros *et al.* (1999) for the LES of the shock/turbulence interaction using a second-order finite-volume scheme. Similar to this analysis, we have identified that the numerical dissipation mainly occurs in the upwind scheme region and the SGS dissipation is the dominant one away from the upwind scheme region. The ratio of the total numerical energy dissipation and the total SGS energy dissipation in the flow field is less than 1 %, consistent with the fraction of grid points occupied by the upwind flux. Furthermore, to justify the use of the numerical method for the present LES, additional analysis based on some quantities, such as the resolved energy spectrum and turbulent fluctuations, will be discussed in the following section.

In this study, the initial and boundary conditions are presented as follows. The initial condition is set as the free-stream quantities. The far-field boundary conditions are treated by local one-dimensional Riemann-invariants, which were designed by Thomas & Salas (1986) for studying transonic flow over a body and were extensively examined and found to be reliable for transonic flows over lifting aerofoils and wings (e.g. Hafez & Wahba 2007). No-slip and adiabatic conditions are applied on the cylinder surface. A periodic condition is used in the spanwise direction of the cylinder.

3. Computational overview and validation

3.1. *Computational overview*

As shown in figure 1, the diameter of the wavy cylinder varies sinusoidally along its spanwise direction. The geometry of the wavy cylinders is described by

$$D_y = D + 2A\cos\left(\frac{2\pi y}{\lambda}\right), \tag{3.1}$$

where D_y denotes the local diameter of the wavy cylinder and varies in the spanwise direction y and A and λ represent the amplitude and wavelength of the wavy surface,

respectively. The mean diameter D is defined by

$$D = \frac{D_{min} + D_{max}}{2}, \tag{3.2}$$

where D_{min} and D_{max} represent the minimum and maximum local diameter of the wavy cylinder and are called 'node' and 'saddle', respectively. The 'middle' is also defined at the midpoint position between nodal and saddle planes. The diameter of the middle cross-section is equal to the mean diameter D.

The parameters used in this study are selected based on some typical experiments for the incompressible flow over a wavy cylinder (e.g. Lam *et al.* 2004*a*,*b*) and for the compressible flow over a circular cylinder (Macha 1977; Murthy & Rose 1978; Rodriguez 1984). The amplitude, A, and wavelength, λ, of the wavy cylinder in figure 1 are chosen as $0.1D$ and $2D$, respectively, consistent with an effective flow control for mean drag and fluctuating lift reduction (Lam *et al.* 2004*a*). For comparison and code validation against experimental data, the compressible flow past a corresponding circular cylinder is also investigated here. Some experiments on the transonic flow past a circular cylinder (Macha 1977; Murthy & Rose 1978; Rodriguez 1984) have been performed for the parameters, such as the free-stream Mach number $M_\infty = 0.75$ and the Reynolds number $Re = 1.7 \times 10^5 - 3.4 \times 10^5$ (Rodriguez 1984). Here, we choose the free-stream Mach number as 0.75 and the Reynolds number based on the mean diameter of the wavy cylinder as 2×10^5.

The grids are of O-type with a far-field boundary at $50D$ away from the cylinder in the (x, z) plane, which is large enough to ensure a reliable treatment of the far-field boundary condition, and grid stretching is employed to increase the grid resolutions near the surface and in the wake region, ensuring that there are at least 40 nodes in the vorticity thickness over the surface in the attached boundary-layer region. An orthogonal grid distribution in the meridian plane is obtained by a conformal mapping technique. For the corresponding circular cylinder, the spanwise grid is divided uniformly. The spanwise length is chosen as twice the wavelength of the wavy cylinder (i.e. $4D$). To justify the choice of this length, the two-point correlations are calculated in terms of the formulation (Pirozzoli, Grasso & Gatski 2004). Figure 2 shows the two-point correlations $R_{\alpha\alpha}(r_y)$ in the spanwise direction (i.e. y-direction), where α represents the fluctuations of any one of the velocity components $\tilde{u}_i$ (or $\tilde{u}$, $\tilde{v}$ and $\tilde{w}$). The correlations decay towards zero which means that the two-point correlations are sufficiently decorrelated over a distance $2D$, thus ensuring that the computational domain in the spanwise direction is sufficiently wide not to inhibit the turbulence dynamics.

To assess the effects of grid resolution and time step on the calculated results, three typical cases with different grid resolutions and time steps as well as the relevant main characteristics are listed in table 1. Detailed comparisons of the calculated results using different computational conditions will be given in § 3.2. Moreover, the present code is equipped with a multi-block domain decomposition feature to facilitate parallel processing in a distributed computing environment. The present computational domain is divided into 32 subdomains for parallel processing. The computed time elapsed is at least $400D/U_\infty$ to obtain statistically meaningful turbulence properties in the temporal average operation.

Based on the time-dependent resolved density, $\bar{\rho}$, pressure, $\bar{p}$, temperature, $\tilde{T}$ and velocity, $\tilde{u}_i$, several averaging operations will be needed. To clearly present the post-process, some symbols used in this paper are introduced as follows: $\langle\ \rangle$ means the average in time (after careful elimination of the transient part of their time-dependent variations) as well as in spatial phase along the spanwise direction for the wavy

	Case	Grid	$U_\infty \Delta t/D$	Wavy	Circular	EXP-1	EXP-2	EXP-3
$\langle C_D \rangle_t$	1	$257 \times 257 \times 61$	0.006	1.167	1.572			
	2	$385 \times 385 \times 81$	0.004	1.162	1.568	1.618	1.5	1.5–1.6
	3	$513 \times 513 \times 121$	0.002	1.162	1.568			
C_{Lrms}	1	$257 \times 257 \times 61$	0.006	0.011	0.250			
	2	$385 \times 385 \times 81$	0.004	0.012	0.254	0.253	–	–
	3	$513 \times 513 \times 121$	0.002	0.012	0.254			
St	1	$257 \times 257 \times 61$	0.006	0.165	0.180			
	2	$385 \times 385 \times 81$	0.004	0.170	0.190	0.2	0.18	–
	3	$513 \times 513 \times 121$	0.002	0.170	0.190			

TABLE 1. Comparison of the calculated results with experimental data for a circular cylinder and validation of the results with different grid resolutions and time steps, i.e. cases 1–3. Here, EXP-1 represents the experimental data from Rodriguez (1984) for $M_\infty = 0.75$ and $Re = 1.7 \times 10^5$–3.4×10^5, EXP-2 from Murthy & Rose (1978) for $M_\infty = 0.8$ and $Re = 1.66 \times 10^5$ and EXP-3 from Macha (1977) for $M_\infty = 0.8$ and $Re = 10^5$–10^6.

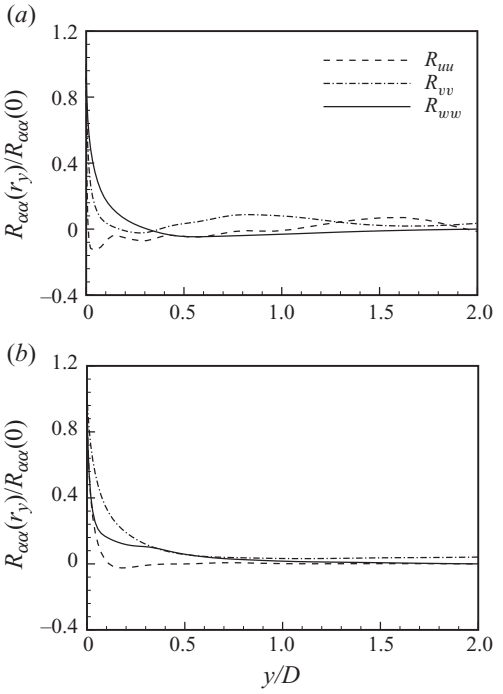

FIGURE 2. Distributions of the two-point correlations of the wavy cylinder flow at two positions at $z/D = 0$ and (*a*) $x/D = 0.7$ and (*b*) $x/D = 2.0$.

cylinder or in the spanwise direction for the circular cylinder, and $\{\phi\} = \langle \bar{\rho}\phi \rangle / \langle \bar{\rho} \rangle$ with a variable ϕ. Then, their fluctuations are obtained as (Garnier, Sagaut & Deville 2002) $\rho' = \bar{\rho} - \langle \bar{\rho} \rangle$, $p' = \bar{p} - \langle \bar{p} \rangle$, $T'' = \tilde{T} - \{\tilde{T}\}$ and $u_i'' = \tilde{u}_i - \{\tilde{u}_i\}$, respectively.

3.2. *Validation*

To validate the present simulation, we first consider the compressible flow over a circular cylinder and compare numerical results and experimental data (Macha 1977;

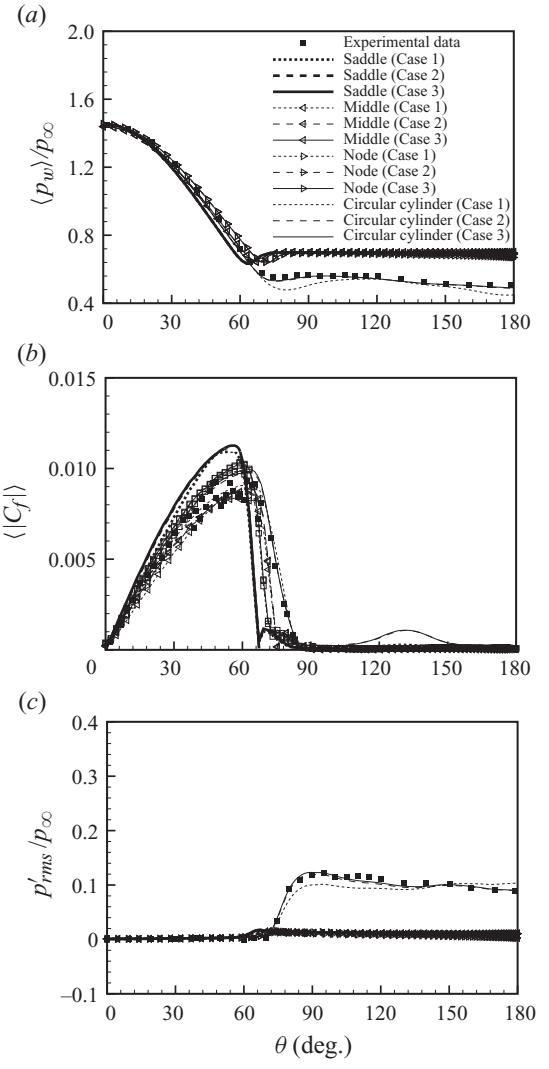

FIGURE 3. Comparison of the calculated results with experimental data for a circular cylinder and validation of the results with different grid resolutions and time steps (i.e. cases 1–3) given in table 1: (*a*) mean wall pressure $\langle p_w \rangle$ with the experimental data (Rodriguez 1984), (*b*) skin friction coefficient $\langle |C_f| \rangle$ with the experimental data (Murthy & Rose 1978) and (*c*) root-mean-square (r.m.s.) value of pressure fluctuation p'_{rms} with the experimental data (Rodriguez 1984). Here, θ increases from the front point of the cylinder in the clockwise direction.

Murthy & Rose 1978; Rodriguez 1984) in terms of the mean pressure, pressure fluctuation and skin friction on the cylinder.

Figure 3 shows the distributions of mean wall pressure $\langle p_w \rangle$, friction coefficient $\langle C_f \rangle$ and pressure fluctuation p'_{rms} on the circular cylinder and their comparisons with the experimental data (Murthy & Rose 1978; Rodriguez 1984). Moreover, validation of the results predicted by different grid resolutions and time steps (i.e. cases 1–3) listed in table 1 is also performed. It is exhibited that the results for cases 2 and 3 compare favourably with the experimental data.

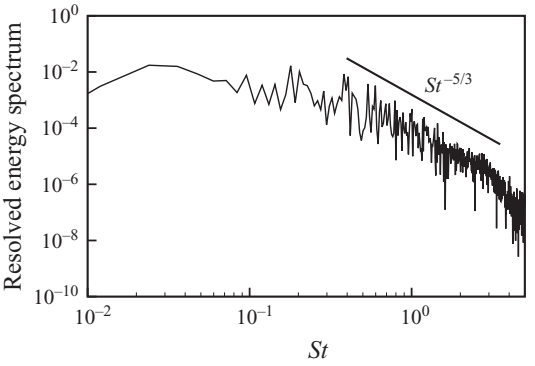

FIGURE 4. Resolved energy spectrum at a location behind the wavy cylinder.

Even though experimental data on the compressible flow over a wavy cylinder are not available yet, assessments of the effect of grid resolution and time step on the calculated solutions are performed. The distributions of mean wall pressure, $\langle p_w \rangle$, friction coefficient, $\langle C_f \rangle$, and pressure fluctuation, p'_{rms}, on the wavy cylinder at the saddle, middle and nodal positions are shown in figure 3. The time-average drag coefficient, $\langle C_D \rangle_t$, lift fluctuation, C_{Lrms}, and Strouhal number are also given in table 1. We have identified that the results for cases 2 and 3 collapse together, indicating a reasonable convergence for the grid resolution and time step. To make the prediction accurate, the results given below were calculated using the parameters in case 3, i.e. the grid number $513 \times 513 \times 121$ in the radial, azimuthal and spanwise direction, respectively, and time step $0.002D/U_\infty$.

On the other hand, the resolved energy spectrum obtained using the parameters in case 3 is shown in figure 4. The resolved scales seem to reach an inertial subrange, reasonably close to $St^{-5/3}$ scaling (Kawai & Fujii 2005). The spatial spectrum can be approximately obtained using Taylor's hypothesis which is limited to homogeneous turbulence with small turbulence intensity (Pope 2000). The illustrated slope indicates that the present calculation can reliably capture the turbulence spectrum. Moreover, the resolved energy spectra obtained by the present numerical method were also examined in some previous investigations (e.g. Wang *et al.* 2007; Chen *et al.* 2010*a*).

Further, the present numerical strategy has already been applied with success to a wide range of turbulent flows such as the compressible turbulent swirling flows injected into a coaxial dump chamber (Lu *et al.* 2005), transonic flows over a circular cylinder (Xu *et al.* 2009*a*; Xu, Chen & Lu 2009*b*) and past an aerofoil (Chen *et al.* 2010*a*) and supersonic flow past a hemispherical nose with an opposing jet (Chen, Xu & Lu 2010*b*). We have carefully examined the physical model and numerical approach used in this study and have verified that the calculated results are reliable.

4. Results and discussion

4.1. *Force behaviours*

4.1.1. *Reduction of mean and fluctuating force*

The features of the forces exerted on a wavy cylinder are an important issue related to the control of flow over a bluff body (e.g. Oertel & Affiliation 1990; Choi *et al.* 2008). Figures 5(*a*) and 5(*b*) show the time-dependent lift and drag coefficients C_L and C_D on the wavy and circular cylinder, respectively. It is seen that obvious reduction of

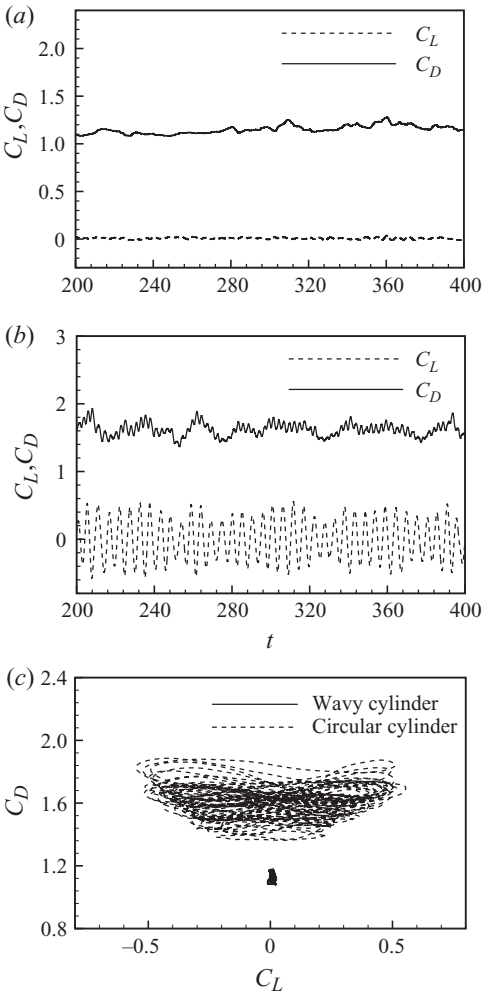

FIGURE 5. Time-dependent lift and drag coefficients on the wavy cylinder (*a*) and circular cylinder (*b*) as well as the phase-space plot of the force components (*c*).

mean drag and fluctuating lift on the wavy cylinder occurs with respect to the ones on the circular cylinder. To clearly compare the time-dependent forces on the cylinders, the phase-space plots of the force components (C_L, C_D) are shown in figure 5(*c*). The diagram of force components on the wavy cylinder is limited to only a local region, indicating that the force fluctuation is significantly suppressed.

Usually, the force fluctuation on a cylinder is associated with the vortex shedding in the wake (e.g. Oertel & Affiliation 1990; Owen & Bearman 2001). To identify the frequency of vortex shedding, the power spectral densities of the time-dependent lift coefficient of the wavy and circular cylinder are shown in figure 6. The characteristic Strouhal number is defined as $St = fD/U_\infty$ with f being the frequency. As exhibited in figure 6 for the circular cylinder, the primary frequency corresponding to the highest peak is approximately 0.19, consistent with experimental data in the range 0.18–0.2 (Murthy & Rose 1978; Rodriguez 1984). The spectral peaks for the wavy cylinder are relatively weak, indicating an almost complete suppression of flow unsteadiness.

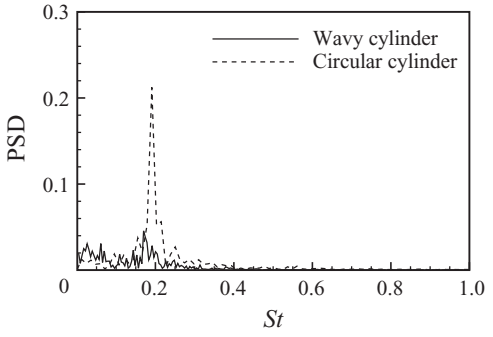

FIGURE 6. Profiles of power spectral density of time-dependent lift coefficient for the wavy and circular cylinder.

To assess quantitatively the reduction of mean drag and fluctuating lift, table 1 shows the time-average drag coefficient $\langle C_D \rangle_t$, the root-mean-square (r.m.s.) value of lift fluctuation C_{Lrms} and the Strouhal number as well as their comparisons with some typical experimental data. We firstly compare with the values of $\langle C_D \rangle_t$ of the two cylinders and note that the $\langle C_D \rangle_t$ of the wavy cylinder is less than that of the circular cylinder with a drag reduction up to 26 %. Then, compared with the values of C_{Lrms}, it is reasonably identified that the fluctuating force on the wavy cylinder is significantly suppressed.

The characteristics of the reduction of mean and fluctuating forces for the incompressible flow past wavy cylinders have been well studied experimentally and numerically (e.g. Lam *et al.* 2004*a*,*b*; Lee & Nguyen 2007; Lam & Lin 2008, 2009). An effective drag reduction about 20 % is obtained with optimal wavelength and amplitude of a wavy cylinder (Lam *et al.* 2004*a*). Even though the wavelength and amplitude calculated in this study may not correspond to the optimal values, the drag reduction is around 26 % given in table 1. The compressible flow past a wavy cylinder can reduce drag more effectively in comparison with the incompressible flow. Therefore, the mechanisms underlying the compressible flow are of great interest for detailed studies. We can foresee that some mechanisms may be similar to those for the incompressible flow past a wavy cylinder, such as the 3D effect on the shear-layer instability, and others could be associated with the compressible effects, such as suppression of shock/turbulence interaction. Thus, we will mainly pay attention to the relevant mechanisms in this complex flow.

4.1.2. *Pressure and friction on the surface*

The forces on the cylinder are contributed by the pressure and viscous shear stress, respectively. To understand their connections to the reduction of mean and fluctuating forces on the wavy cylinder, figure 3 shows the mean pressure and its fluctuation as well as friction on the cylinder surface. As shown in figure 3(*a*), the pressure distributions at the nodal, middle and saddle locations nearly collapse together, especially in the base range of the cylinder with a nearly unchanged value, and are obviously higher than that of the corresponding circular cylinder. As the Reynolds number considered here is $O(10^5)$, the pressure force plays a dominant role in the total forces on the cylinder. Thus, we can learn that the higher base pressure is mainly responsible for the drag reduction.

As shown in figure 3(*b*), the skin friction mainly exists in the attached flow region over the surface, drops quickly before the mean separation location, and approaches

very small values in the base region of the cylinder. The peak value of skin friction at the saddle location is obviously higher than the one at the nodal location. This behaviour is related to the flow phenomenon that the spanwise flow is from the nodal plane towards the saddle plane on both sides of the wavy cylinder before the flow separation, which will be discussed in detail in § 4.3. We have carefully examined the total skin friction on the wavy cylinder which is somewhat less than that on the circular cylinder, related to the fact that the mean separation on the wavy cylinder is earlier than that on the circular cylinder. Further, it is reasonably identified that the contribution on the drag reduction due to the skin friction effect is negligibly small relative to the pressure force effect.

Based on the above analysis, the forces on the cylinder are mainly associated with the pressure distribution. Thus, the pressure fluctuation on the surface (i.e. p'_{rms}) is shown in figure 3(c). In the attached flow region, the pressure fluctuation nearly vanishes. The peak value occurs around the mean separation location, which is related to the fluctuating displacement of instantaneous separation (Batham 1973; Shvets 1983). The pressure fluctuation obviously exists in the base region of the cylinder. From the distributions of p'_{rms} in figure 3(c), it is identified that the pressure fluctuation on the wavy cylinder is significantly suppressed in the base region, resulting in a reduction of C_{Lrms} on the wavy cylinder listed in table 1.

4.1.3. *Analysis of drag decomposition*

The forces exerted on a body for viscous compressible flow around it depend strongly on the dynamic processes, such as shearing and compressing ones. To understand the mechanisms underlying the compressible flow past the cylinders, the force expression based on derivative-moment transformations (Wu, Ma & Zhou 2006; Wu *et al.* 2007) is used to analyse the drag-force contributions. Let V_f be a 3D compressible fluid domain surrounding a rigid and stationary body, B, and bounded externally by an arbitrary control surface, Σ, then the force formulation in terms of the resolved variables is expressed as (Wu *et al.* 2006)

$$\boldsymbol{F} = -\frac{1}{2}\int_{V_f} \boldsymbol{x}\times\nabla\times\left(\bar{\rho}\frac{\partial\tilde{\boldsymbol{u}}}{\partial t}\right)\mathrm{d}V - \int_{V_f}\left(\bar{\rho}\tilde{\boldsymbol{\omega}}\times\tilde{\boldsymbol{u}} - \frac{1}{2}(\tilde{\boldsymbol{u}}\cdot\tilde{\boldsymbol{u}})\nabla\bar{\rho}\right)\mathrm{d}V$$
$$-\frac{1}{2}\int_{\partial V_f}\boldsymbol{x}\times\left[\boldsymbol{n}\times\left(\bar{\rho}\tilde{\boldsymbol{\omega}}\times\tilde{\boldsymbol{u}} - \frac{1}{2}(\tilde{\boldsymbol{u}}\cdot\tilde{\boldsymbol{u}})\nabla\bar{\rho}\right)\right]\mathrm{d}S + \boldsymbol{F}_\Sigma + \boldsymbol{F}_A, \quad (4.1)$$

where $\tilde{\boldsymbol{\omega}} = \nabla\times\tilde{\boldsymbol{u}}$ is the vorticity, $\boldsymbol{x}$ denotes the spatial vector and $\partial V_f = \partial B + \Sigma$ is the surrounding boundary of V_f with ∂B being the body surface. The boundary integral in (4.1)

$$\boldsymbol{F}_\Sigma = -\frac{1}{2}\int_\Sigma \boldsymbol{x}\times[\boldsymbol{n}\times(\nabla\times\tilde{\mu}\tilde{\boldsymbol{\omega}})]\,\mathrm{d}S + \int_\Sigma \tilde{\mu}\tilde{\boldsymbol{\omega}}\times\boldsymbol{n}\,\mathrm{d}S, \quad (4.2)$$

is the contribution to the force of the flow structures on the finite control surface Σ, which is a pure viscous effect.

We imposed a periodic condition in the spanwise direction in the present calculation, so that only a finite length of the cylinder lies in the computational domain. V_f is a doubly connected domain, and both the control surface and body surface are open surfaces. Then an additional term due to the open control surface in (4.1) is expressed as (Wu *et al.* 2006)

$$\boldsymbol{F}_A = \frac{1}{2}\int_{\partial B}\boldsymbol{x}\times(\bar{p}\mathrm{d}\boldsymbol{x} - 2\tilde{\mu}\tilde{\boldsymbol{\omega}}\times\mathrm{d}\boldsymbol{x}) + 2\int_{\partial B}\tilde{\mu}\tilde{\boldsymbol{u}}\times\mathrm{d}\boldsymbol{x}. \quad (4.3)$$

As a check, when Σ shrinks to coincide with ∂B so that all volume integrals over V_f disappear, (4.1) degenerates to the boundary vorticity flux (BVF) based force expression for an open body surface (Wu *et al.* 2007).

According to the analysis of force decomposition (Wu *et al.* 2006), the terms in (4.1), i.e. $-(\tilde{\boldsymbol{u}}\cdot\tilde{\boldsymbol{u}})\nabla\bar{\rho}/2$ and $\bar{\rho}\tilde{\boldsymbol{\omega}}\times\tilde{\boldsymbol{u}}$, are related to the compressing effect and the vortex force, respectively. Then, the force components corresponding to the two terms are given as

$$\boldsymbol{F}_C = \int_{V_f} \frac{1}{2}(\tilde{\boldsymbol{u}}\cdot\tilde{\boldsymbol{u}})\nabla\bar{\rho}\,\mathrm{d}V + \frac{1}{2}\int_{\partial V_f} \boldsymbol{x}\times\boldsymbol{n}\times\left(\frac{1}{2}(\tilde{\boldsymbol{u}}\cdot\tilde{\boldsymbol{u}})\nabla\bar{\rho}\right)\mathrm{d}S, \tag{4.4}$$

$$\boldsymbol{F}_V = -\int_{V_f} (\bar{\rho}\tilde{\boldsymbol{\omega}}\times\tilde{\boldsymbol{u}})\,\mathrm{d}V - \frac{1}{2}\int_{\partial V_f} \boldsymbol{x}\times[\boldsymbol{n}\times(\bar{\rho}\tilde{\boldsymbol{\omega}}\times\tilde{\boldsymbol{u}})]\,\mathrm{d}S. \tag{4.5}$$

Here we use (4.1) to analyse the drag reduction because of the compressing and shearing processes. The boundary integral (4.2) is calculated. Since this term is a pure viscous effect, its value is negligibly small when the control surface Σ is chosen as over $40D$ away from the cylinder in the cross-section plane, which is used to calculate other terms in (4.1). The term due to the open control surface (4.3) contributes approximately half the total drag force for high-Reynolds-number flow, consistent with the result for viscous flow over a circular cylinder (Wu *et al.* 2007).

Further, we mainly discuss the drag contributions related to the compressing effect and the vortex force. The mean values of drag coefficient using (4.4) are obtained as approximately 0.35 and 0.45 for the wavy and circular cylinder, respectively; the drag reduction due to the compressing effect is around 22 %. Similarly, the drag coefficient values due to the vortex force (4.5) are 0.24 and 0.34 for the wavy and circular cylinder, and the corresponding drag reduction is approximately 29 %. Then, we may learn that the drag reduction due to the shearing process prevails over that due to the compressing process in this flow. The underlying mechanisms will be discussed below. Moreover, compared with the mean values obtained by (4.4) and (4.5) for the wavy cylinder or the circular cylinder, it is found that the contribution of the compressing effect is higher than that of the vortex force. This finding was also confirmed for transonic flow around a circular cylinder or a sphere (Chang & Lei 1996).

4.2. *Flow structures and turbulent fluctuations*

4.2.1. *Boundary vorticity flux and vortical structures*

For this compressible flow past the cylinder, the shearing and compressing processes should be coupled to affect the overall flow characteristics. Thus, the mechanisms relevant to the control of flow past a wavy cylinder are also associated with the two processes and will be analysed from the body surface to the flow field based on both the processes.

A quantitative understanding of the connection of the two processes on the cylinder surface is of fundamental significance and may improve our capabilities for flow analysis and control. The BVF represents an on-surface dynamic process which causes the formation of vortical structures and is also related to the local compressing process, but itself is not a flow structure (e.g. Wu *et al.* 2006, 2007). As the BVF is always of $O(1)$ even if $Re \gg 1$, the $o(1)$ viscous terms are often neglected at large Re to focus on the key physics (Wu *et al.* 2006). Thus, for the present flow with a higher Re, the BVF can be approximately expressed as

$$\boldsymbol{\sigma} = \frac{\tilde{\mu}}{\bar{\rho}}\frac{\partial\tilde{\boldsymbol{\omega}}}{\partial n} \simeq \frac{1}{\bar{\rho}}\boldsymbol{n}\times\nabla\bar{p}, \tag{4.6}$$

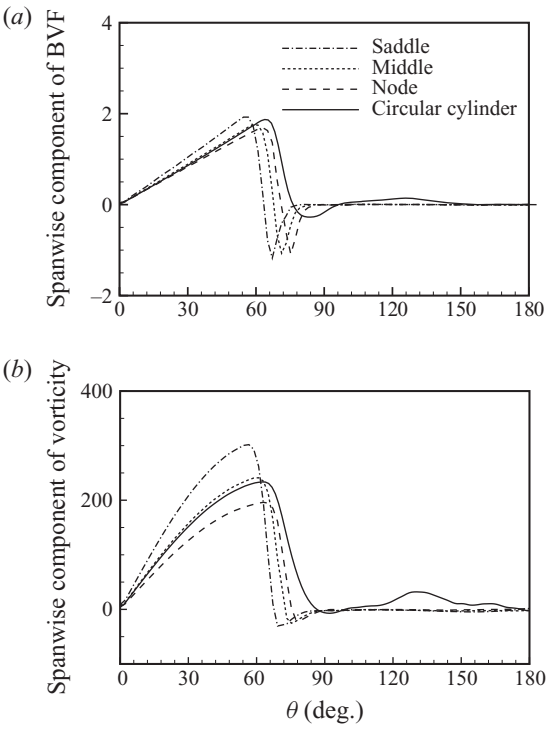

FIGURE 7. Distributions of the mean spanwise BVF (*a*) and vorticity (*b*).

where $\boldsymbol{n}$ represents the inward normal unit vector on a solid wall. Lighthill (1963) was the first to interpret (4.6) as the measure of vorticity creation and emphasized the role of tangent pressure gradient. Thus, we can learn that the BVF is in turn dominated by the tangent pressure gradient, which measures the local dynamics of the compressing process (Wu *et al.* 2006). Once that tangent pressure gradient is formed on the surface, it becomes a cause of new vorticity, which measures the local dynamics of the shearing process.

After we examine the σ components, it is identified that the spanwise BVF is dominant. The distributions of mean spanwise BVF and vorticity components are shown in figures 7(*a*) and 7(*b*), respectively. The BVF occurs obviously in the attached flow region and drops quickly at the mean flow separation location. Moreover, in the attached flow region, the higher BVF at the saddle position corresponds reasonably well to the larger vorticity, consistent with the larger skin friction in figure 3(*b*). Similar behaviour is also identified at the nodal position. The peak value of BVF on the circular cylinder is somewhat larger than the one on the wavy cylinder at the middle position, which is associated with the tangent pressure gradient (4.6) induced by the formation of a shock wave over the circular cylinder discussed below. In addition, we also calculated the right-hand side of (4.6) and confirmed that its profile (not shown here) collapses with the BVF.

The vortical structures in the near wake are closely associated with the dynamic characteristics on a body (Wu *et al.* 2007) and flow control over a bluff body (Choi *et al.* 2008). To exhibit the coherent structures in the flow field, figure 8 shows instantaneous snapshots of the flow field depicted by isosurface of the Q criterion

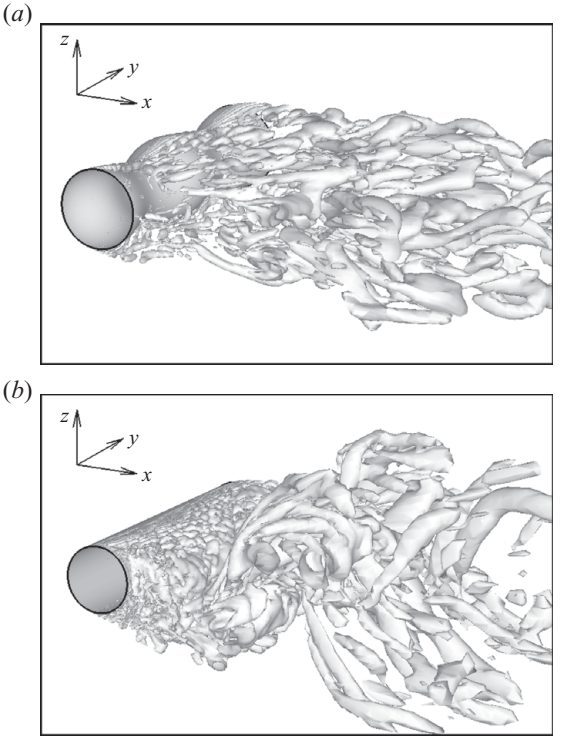

FIGURE 8. Vortical structures by isosurface of the Q-criterion ($Q = 1$): (a) wavy cylinder and (b) circular cylinder.

(Jeong & Hussain 1995)

$$Q = -\tfrac{1}{2}(\|\boldsymbol{S}\|^2 - \|\boldsymbol{\Omega}\|^2), \tag{4.7}$$

where $\boldsymbol{S}$ and $\boldsymbol{\Omega}$ denote the strain and the rotation tensor, respectively. A positive value of Q presents the regions in which the rotation exceeds the strain. It must be recalled that the criterion (4.7) is only applied to the resolved scales obtained by LES and that the vortical structures could be different if the whole flow field was considered (Simon *et al.* 2007). Based on careful comparison of the structures behind the cylinders in figure 8, some prominent differences of the vortical structures in the near wake are identified. The vortical structures near the base region of the wavy cylinder are significantly less vigorous than those of the circular cylinder. The vortex roll up of the separated shear layer from the wavy cylinder is delayed to a downstream position, while this phenomenon occurs in the initial stage of the shear-layer shed from the circular cylinder.

To clearly demonstrate the vortex structures in the near wake, figure 9 shows the isocontours of mean vorticity magnitude $\langle|\tilde{\boldsymbol{\omega}}|\rangle$, for clarity, in the cross-section planes. It is observed that the near wake structures behind the wavy cylinder have been modified significantly compared with the circular cylinder flow. From the patterns behind the wavy cylinder, the separated free shear layers are relatively more stable and then roll up into vortices in the further downstream positions, leading to a reduction of the suction near the base region of the wavy cylinder. This feature is reasonably related to the higher-base-pressure distribution in figure 3(a). Moreover, the mechanisms of the more stable shear-layers shed from the wavy cylinder are of

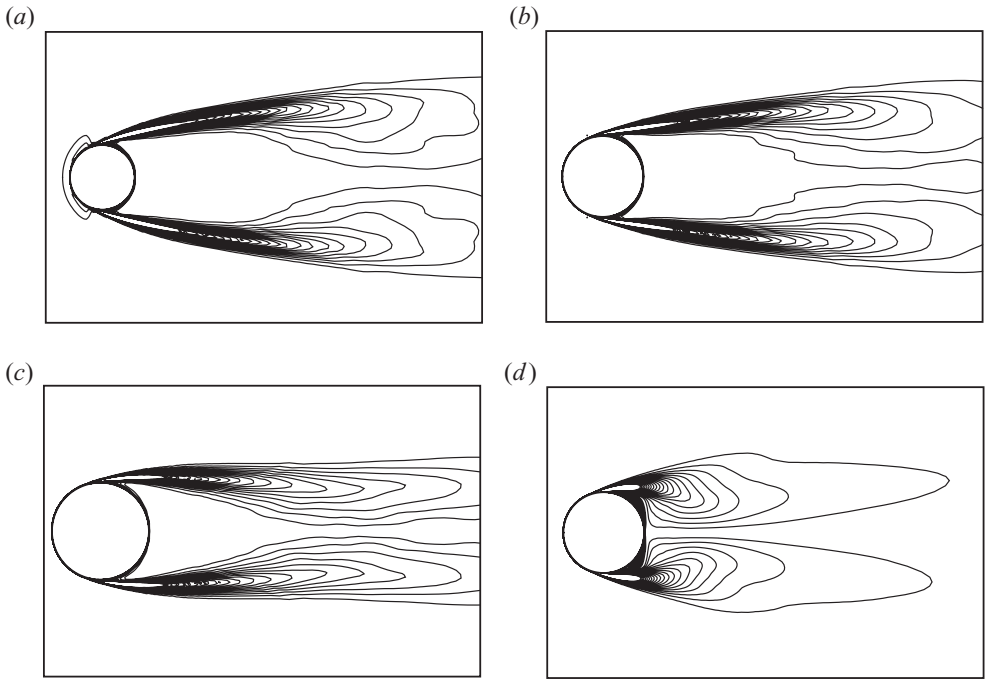

FIGURE 9. The isocontours of mean vorticity magnitude in the cross-section planes: (*a*) saddle, (*b*) middle, (*c*) nodal plane of wavy cylinder and (*d*) mid-spanwise plane of circular cylinder.

importance in understanding the flow characteristics and will be discussed further in § 4.3.

4.2.2. *Shock waves and shocklets and their elimination around the wavy cylinder*

For transonic flow past a circular cylinder, there exist an array of intricate phenomena, e.g. moving shock waves, LSZs and shocklets, and shock/turbulent flow interaction (Xu *et al.* 2009*a*). To assess the passive control of the compressible flow past a wavy cylinder, the existence of these phenomena relevant to the compressible effect is further discussed for the wavy and circular cylinders, which will be of help in understanding the mechanisms of the drag reduction and fluctuating force suppression.

The instantaneous isocontours of local Mach number, M_l, and velocity divergence or dilatation are shown in figures 10 and 11 in the cross-section planes, respectively. Firstly we take an overview on the flow phenomena around the cylinders. For the circular cylinder flow, as exhibited in figure 10(*d*), the moving shock waves are formed over the cylinder and in the near wake, resulting in complex shock/boundary layer interaction and shock/wake interaction (Xu *et al.* 2009*a*,*b*). These flow phenomena are consistent with the experimental observations (Rodriguez 1984; Thombi *et al.* 2002). As expected, strong negative dilatation related to the shock occurs in figure 11(*d*). Moreover, the LSZs are intermittently generated in the near wake of the circular cylinder and are associated with the local eddies. The shocklets may also occur in accordance with the stronger LSZs and will be further analysed below.

Correspondingly, after we carefully examine the flow field around the wavy cylinder shown in figure 10(*a–c*), the shocks and shocklets are not detected. The weaker LSZs are intermittently formed only in the outside region of the separated shear

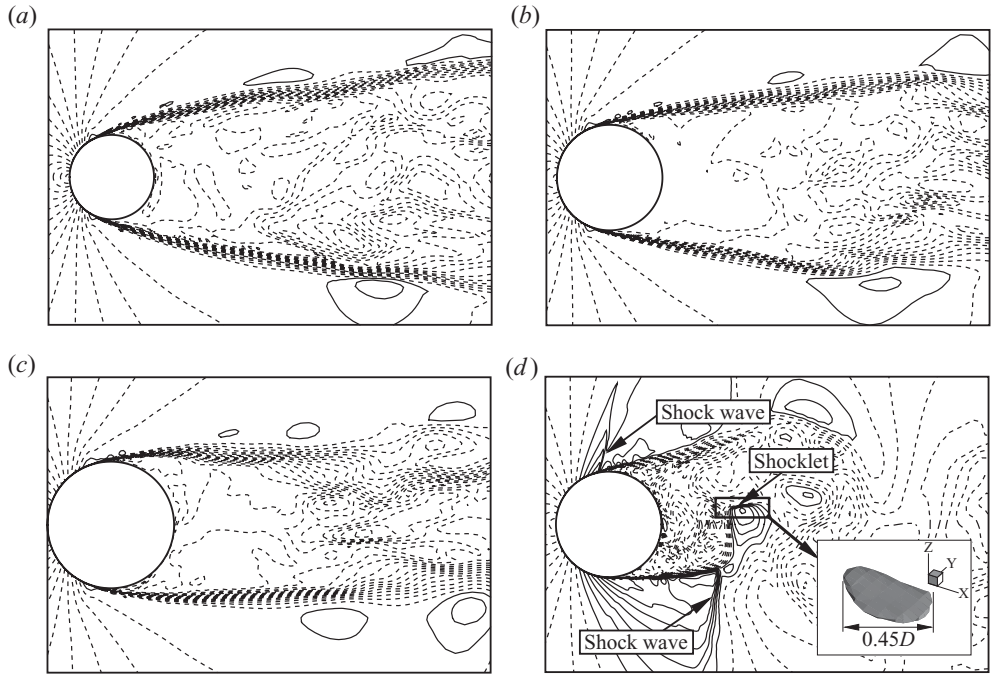

FIGURE 10. Instantaneous isocontours of local Mach number, M_l, in the cross-section planes: (*a*) saddle, (*b*) middle, (*c*) nodal plane of wavy cylinder and (*d*) mid-spanwise plane of circular cylinder; the 3D shocklet surface structure is plotted in the inset. Here, solid lines denote $M_l > 1$ and dashed lines $M_l < 1$.

layers. The elimination of shocks and shocklets around the wavy cylinder plays an important role in the compressible flow control by avoiding the shock-induced pressure drag (Bushnell 2004) and suppressing the force fluctuation. Moreover, shock wave control possesses both fundamental and application importance (e.g. Stanewsky 2001). Following the present findings, the wavy surface may also provide an effective way of shock control, say an airfoil with small amplitude wavy surface for transonic buffet control.

Further, it is identified that the local Mach number in the near wake of the wavy cylinder is even as low as $O(10^{-2})$ in figure 10(*a–c*). This lower-velocity region is closely related to the more stable shear layers. From figure 11(*a–c*), a flow-expansion effect with positive dilatation exists along the shear layers from the saddle and middle position. In contrast, a flow-compression effect occurs along the shear layer from the nodal position and is associated with the flow phenomenon that the spanwise flow is from the saddle plane towards the nodal plane on both sides of the wavy cylinder after the flow separation discussed in § 4.3.

From the preceding description of the moving shock wave on the circular cylinder, it is important to exhibit the relevant intricate flow phenomena including shock/boundary layer interaction and shock-induced flow separation. Figure 12 shows the time development of flow structures using the isocontours of $\partial \bar{p}/\partial x$ (Simon *et al.* 2007) in the mid-spanwise plane of the circular cylinder. Here, we pay attention to the flow evolution over the upper surface. A shock wave is formed on the surface because of upstream-propagating compression waves from the base region. This shock wave moves upstream, while increasing its strength and induces the boundary layer

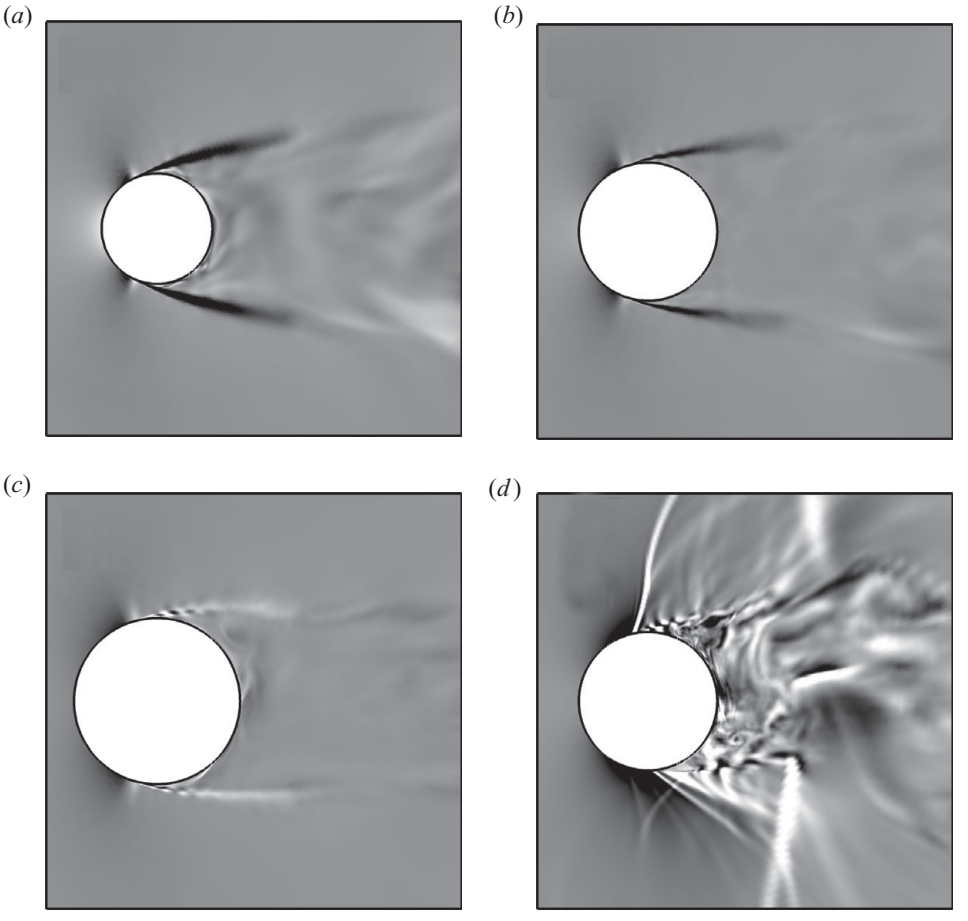

FIGURE 11. Visualizations of instantaneous velocity divergence in the cross-section planes: (*a*) saddle, (*b*) middle, (*c*) nodal plane of wavy cylinder and (*d*) mid-spanwise plane of circular cylinder. Here, bright shades represents negative values and dark shades positive ones.

separation. Then, the shock wave weakens and quickly disappears. This phenomenon is repeated alternately between the upper and lower surfaces of the circular cylinder. Based on our recent work on the transonic flow past a circular-arc airfoil (Chen *et al.* 2010*a*), the shock/boundary layer interaction enhances turbulent fluctuations and stimulates the separated shear layer to become more unstable. In contrast, when the formation of the shock wave is suppressed over the wavy cylinder, it is of help in avoiding shock-induced wave drag and keeping more stable evolution of the shear layers.

We next turn to the existence of shocklets in the near wake of the circular cylinder, as shown in figures 10(*d*) and 11(*d*). Usually, the shocklets are associated with turbulent eddies. Lee, Lele & Moin (1991) used the term 'eddy shocklets' to describe shocks produced by the fluctuating fields of the turbulent eddies. Here, it is interesting to examine the physical structure of shocklets. The region with strong negative dilatation is referred to as a shocklet (e.g. Vreman, Kuerten & Geurts 1995; Freund, Lele & Moin 2000). Additionally, utilizing the locus of the zero crossing of $\nabla^2\bar{\rho}$ is also considered to determine the precise shocklet location (Samtaney, Pulin & Kosović 2001). By means of the approach described in detail by Freund *et al.* (2000), we have identified

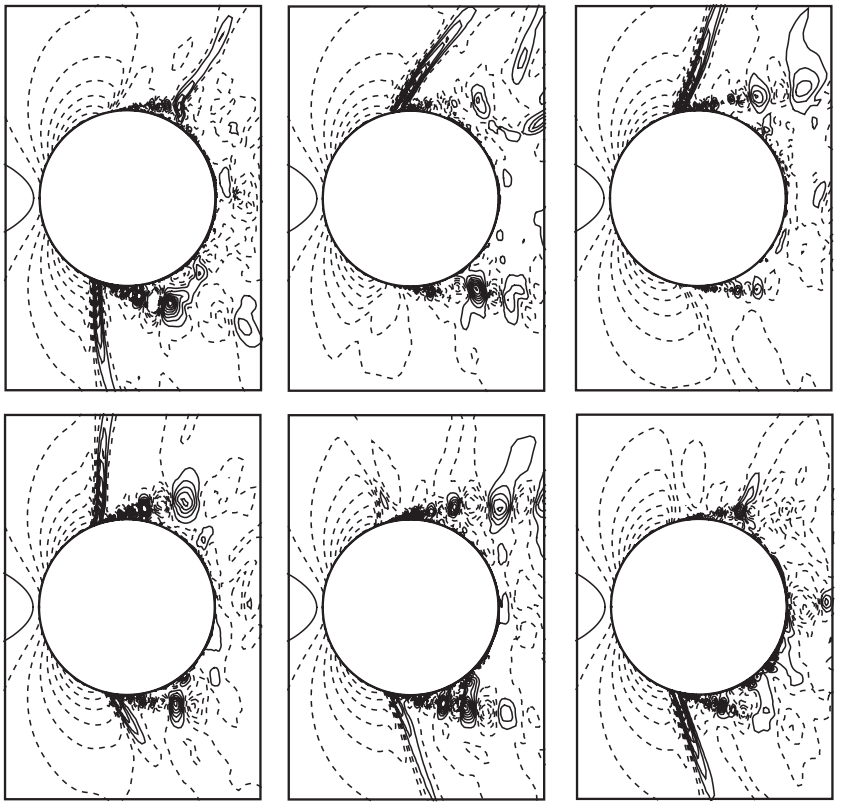

FIGURE 12. Shock wave motion over the circular cylinder depicted by $\partial p/\partial x$ in the mid-spanwise plane with the same time increment. Here, solid lines denote positive values and dashed lines negative ones.

the 3D shocklet surface structure, as typically shown in the inset of figure 10(d), and have confirmed that the change of the flow state across the shocklet satisfies the Rankine–Hugoniot conditions. After examining the shocklet surface structures at different instants and locations, the extracted shocklets exhibit basically a curved dish-like structure. Similarly, the shocklets show a curved ribbon-like structure in decaying compressible, isotropic turbulence (Freund *et al.* 2000).

The interaction between the shocklets and turbulence is mutual. The presence of the shocklets in the wake can induce a high level of turbulent fluctuations. The acoustic mode is also prevalent in this region, which is in accordance with the existence of the shocklets (Loginov, Adams & Zheltovodov 2006). As the shocklets in the near wake of the wavy cylinder are eliminated, we can reasonably predict that the turbulent fluctuations may be reduced which will be discussed below.

4.2.3. *Turbulent fluctuations and their suppression behind the wavy cylinder*

Turbulent fluctuations around a body are associated with the fluctuating forces exerted on it (Wu *et al.* 2007). To characterize the turbulent fluctuations around the cylinder, the isocontours of the mean TKE, i.e. $\langle k\rangle = \langle \bar{\rho} u_i'' u_i''\rangle/2$, are shown in figure 13 in the cross-section planes. It is obviously seen that the TKE is negligibly small in the near wake of the wavy cylinder. This feature results in lower fluctuating surface pressure (Nakamura & Igarashi 2008).

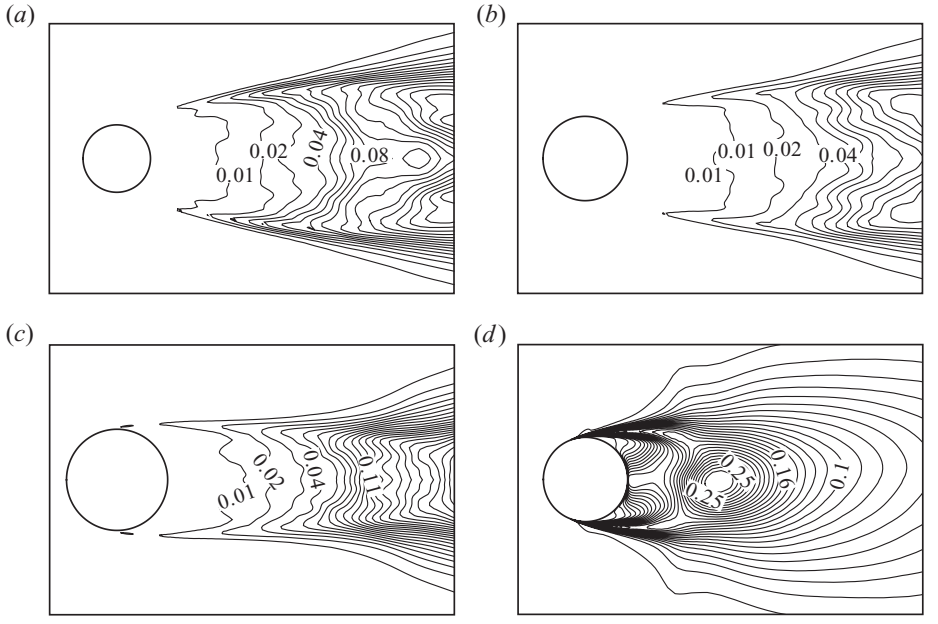

FIGURE 13. The isocontours of mean TKE $\langle k \rangle$, in the cross-section planes: (*a*) saddle, (*b*) middle, (*c*) nodal plane of wavy cylinder and (*d*) mid-spanwise plane of circular cylinder.

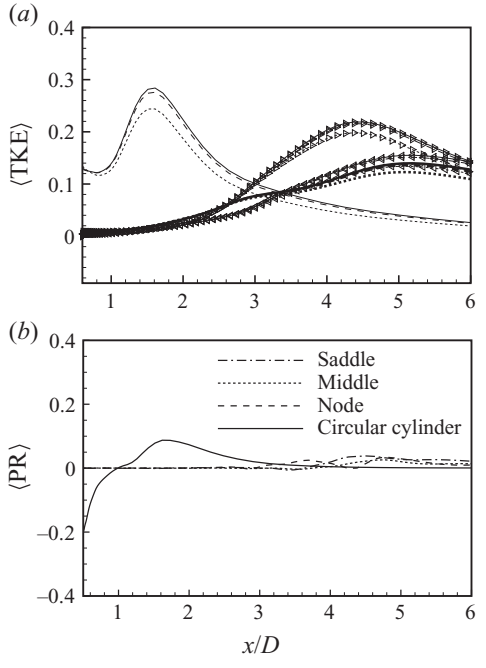

FIGURE 14. Profiles of TKE (*a*) and its production (*b*) along the symmetry line of the cylinder wake. In (*a*), the results with different grid resolutions and time steps (i.e. cases 1–3 in table 1) are plotted for validation and the legend of lines is same as the one in figure 3(*a*).

Further, the profiles of $\langle k \rangle$ and the turbulent production term (i.e. $P = -\langle \bar{\rho} u_i'' u_j'' \rangle \{\tilde{u}_i\}_{,j}$) along the symmetry line of the cylinder wake are shown in figures 14(*a*) and 14(*b*), respectively. From the distributions behind the wavy cylinder,

$\langle k \rangle$ is nearly zero in the range of approximately $x/D < 1.5$, increases gradually, and reaches a maximum in the range of around $x/D = 4.5$. Moreover, the location of the $\langle k \rangle$ peak in the nodal plane occurs earlier and its value is higher than the ones in the saddle and middle planes. Thus, the separated shear layers from the nodal position may become unstable earlier to roll up into mature vortices, consistent with the vorticity patterns in figure 9. Correspondingly, $\langle k \rangle$ reaches its maximum at $x/D = 1.6$ approximately and then decreases gradually behind the circular cylinder. Furthermore, as shown in figure 3, the convergence check based on the forces on the cylinder surface has been performed. The profiles of $\langle k \rangle$ calculated by different grid resolutions and time steps are also shown in figure 14(a) for the convergence check. It is seen that the results for cases 2 and 3 approach each other, indicating that the turbulent fluctuations can be reliably predicted by the grid resolution and time step used in this study.

The turbulent production term is a typical one in the transport equation of TKE. As shown in figure 14(b), the production term behind the wavy cylinder is nearly zero in the range of $x/D < 3$ approximately and exists obviously in $x/D > 3$. It means that the turbulent production is significantly suppressed in the near wake. We have examined other terms in the transport equation of TKE (not shown here) and have identified that they are obviously small behind the wavy cylinder. Further, the negative production distribution behind the circular cylinder is related to the recirculation flow induced by the large-scale vortices. Then, the production term becomes positive and reaches its maximum at approximately $x/D = 1.7$, reasonably corresponding to the location of the $\langle k \rangle$ peak.

To understand the characteristics related to the suppression of turbulent fluctuations behind the wavy cylinder, we may alternatively analyse the underlying reasons for the generation of higher-level turbulent fluctuations behind the circular cylinder. As shown in figure 12, the moving shock on the cylinder surface induces the boundary-layer separation and stimulates the separated shear layer to become more unstable (Chen *et al.* 2010*a*). Then, the vortex roll up of the shear layer quickly happens to form the large-scale vortices near the cylinder, as shown in figure 9(d). We have examined a typical term $(\tilde{\boldsymbol{\omega}} \cdot \nabla)\tilde{\boldsymbol{u}}$ in the transport equation of vorticity, which is related to the mechanism of tilt and stretch of vorticity (Chorin 1994), and have found that a clear distribution (not shown here) occurs in the near wake of the circular cylinder, resulting in the fluctuating fields of turbulent eddies. On the other hand, as shown in figure 10(a), the existence of shocklets can stimulate turbulent fluctuations because of their mutual interaction. Moreover, the shock wave/wake interaction also enhances the turbulent fluctuations (Chen *et al.* 2010*a*). In contrast, as the shocks and shocklets are eliminated around the wavy cylinder, these circumstances that existed in the circular cylinder are avoided, resulting in a significant suppression of the turbulent fluctuations behind the wavy cylinder.

4.3. *The three-dimensional separation and shear-layer evolution*

4.3.1. *The three-dimensional separation on the wavy cylinder*

From the preceding analysis of the flow-field structures and flow characteristics, it is reasonably well understood that the 3D compressible shear-layer development plays an important role in the flow control relevant to the drag reduction and fluctuating force suppression. In order to understand the mechanisms of flow control, we further analyse the 3D separation on the wavy cylinder.

Figure 15 shows the mean separation location on the wavy cylinder surface, corresponding to the resolved skin friction stress vanishing. It is observed that

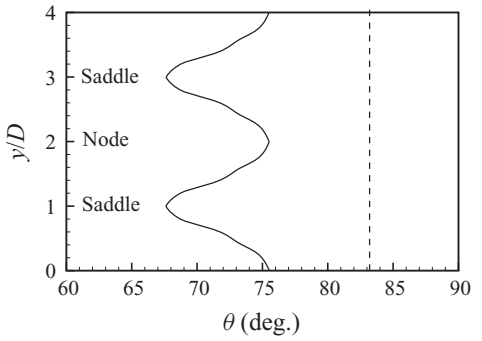

FIGURE 15. Mean separation locations on the surface of wavy cylinder (solid line) and of circular cylinder (dashed line).

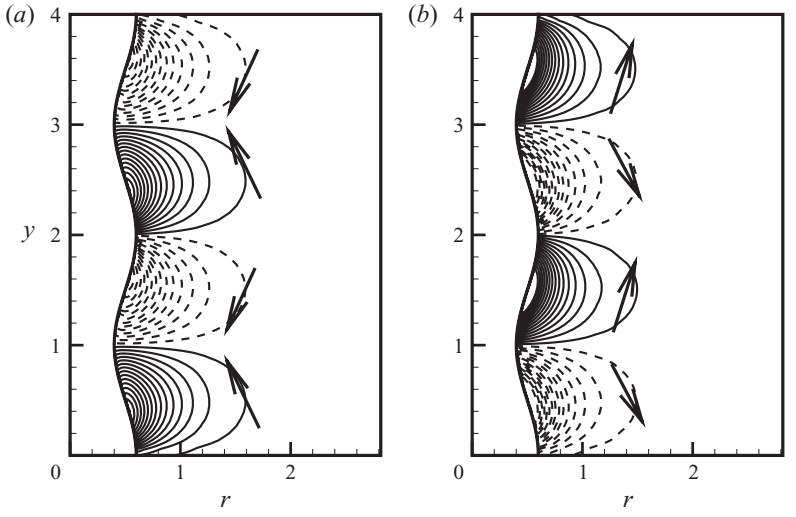

FIGURE 16. The isocontours of mean spanwise velocity component in the meridian planes: (*a*) $\theta = 65.6^\circ$ and (*b*) $\theta = 77.3^\circ$. Here, solid lines denote positive values and dashed lines negative values, and the arrows represent the local flow direction.

the separation happens earliest at the saddle position. For comparison, the mean separation location on the circular cylinder is also predicted and shown in figure 15. The separation from the wavy cylinder is earlier than that from the circular cylinder, consistent with the experimental findings for the incompressible flow past a wavy cylinder (Lam *et al.* 2004*a*,*b*; Zhang *et al.* 2005). The wave-like separation location is likely to result in the 3D shear layers which have an important influence on the evolution of the turbulent wake behind the wavy cylinder.

To exhibit the local flow behaviour near the wavy surface, the isocontours of mean spanwise velocity component are shown in figure 16 in the meridian planes at $\theta = 65.6^\circ$ and 77.3°, corresponding to the plane before and after the separation, respectively. It is seen that the spanwise flow is from the nodal plane towards the saddle plane on both sides of the wavy cylinder at $\theta = 65.6^\circ$ and reverses its direction at $\theta = 77.3^\circ$. It means that the spanwise pressure gradient is formed along the wavy surface, resulting in a cause or on-surface root of new vorticity generation in the azimuthal direction from (4.6). Thus, the corresponding vorticity component is generated and is of help in

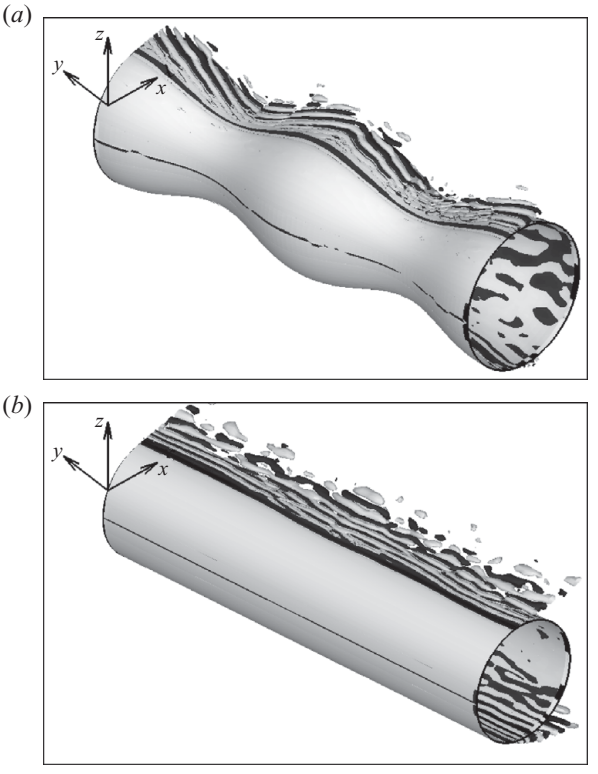

FIGURE 17. Instantaneous snapshot of the spanwise component of the baroclinic term in the transport equation of vorticity: (*a*) wavy cylinder and (*b*) circular cylinder.

the formation of an oblique vortex-shedding mode which may moderate the increase of the amplitude of fluctuation at the shear layer (Prasad & Williamson 1997).

The 3D separation behaviour is associated with the local vorticity dynamics. We have thus examined the terms in the transport equation of vorticity and have noticed that the baroclinic term $(\nabla\bar{\rho}\times\nabla\bar{p})/\bar{\rho}^2$ mainly occurs at the separated shear layers because of the coupled shearing and compressing processes. Figure 17 shows an instantaneous snapshot of the spanwise component of the baroclinic term, which is a dominant component. The oblique and nearly parallel distributions appear over the wavy and circular cylinders, respectively. The oblique distribution tends to generate the oblique vortical perturbation to the separated shear layer, which is of help in its more stable development.

4.3.2. *Characteristics of the separated shear-layer evolution*

As the 3D separation occurs on the wavy cylinder, the characteristics of the separated shear-layer evolution are reasonably related to the mechanisms of the flow control. For the purpose of better understanding the shear-layer evolution, figure 18 shows the topological structure of the shear layer in the near wake in terms of the location of peak shear-stress magnitude (Simon *et al.* 2007). It is seen that the 3D shear layer is formed behind the wavy cylinder. Moreover, figure 19(*a*) shows the locations of the shear layer in the nodal, middle and saddle planes. The transverse location of the shear layer decreases smoothly in the nodal plane and increases in the saddle plane; it means that the wake width shrinking and expanding occur in

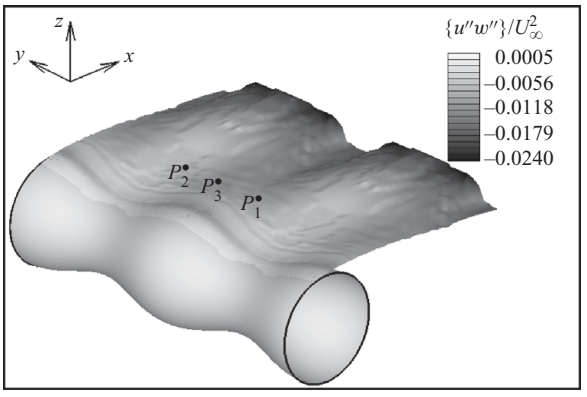

FIGURE 18. Topological structure of shear layer shed from the upper side of the wavy cylinder. Here, the positions P_1, P_2 and P_3 are located in the nodal, saddle and middle planes at $x = 0.95$, respectively.

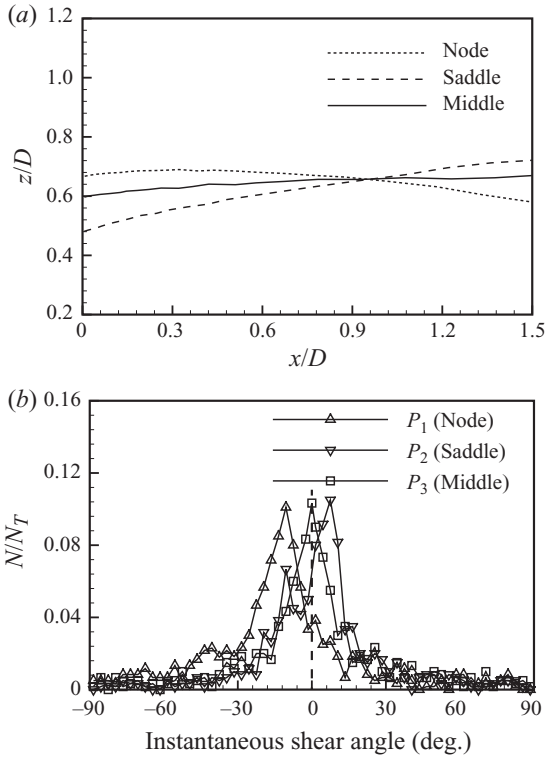

FIGURE 19. Spatial evolution of shear layer: (*a*) transverse locations of shear layer in the nodal, saddle and middle planes and (*b*) PDF of the shear-stress angle, ψ, at P_1, P_2 and P_3 marked in figure 18.

the near wake of the wavy cylinder, consistent with the topological structure shown in figure 18. It is interesting to note that from figure 19(*a*) the transverse location is nearly equal to 0.65 approximately at $x = 0.95$ marked by P_i ($i = 1$–3) in figure 18.

To exhibit the organization of the Reynolds-stress distribution at the shear layer, a shear-stress angle, ψ, is analysed as performed by Herrin & Dutton (1995) and

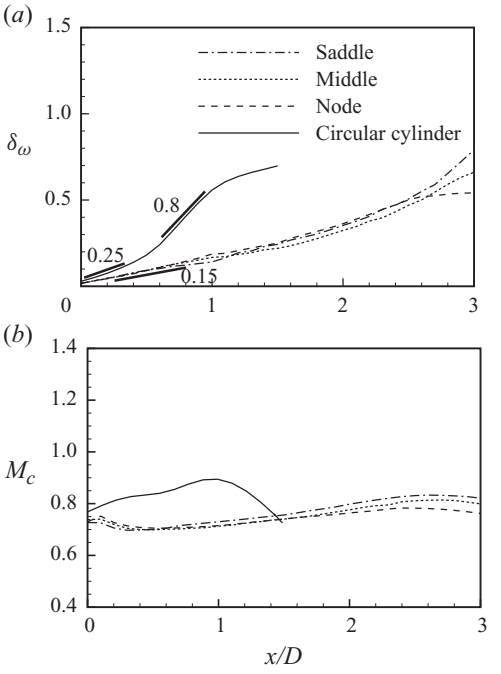

FIGURE 20. Evolution of vorticity thickness (*a*) and convective Mach number (*b*) along the mean shear layers in the saddle, middle and nodal planes of the wavy cylinder and mid-spanwise plane of the circular cylinder.

is defined as $\psi = \arctan(w''/u'')$, where u'' and w'' represent the instantaneous streamwise and transverse velocity fluctuations which are determined through the sampled flow fields. To identify the orientation of the large scale, energy-containing eddies, a quadrant decomposition analysis (Wallace, Eckelmann & Brodkey 1972; Willmarth & Lu 1972; Lu & Willmarth 1973) is used. Based on the definition of ψ, $\psi < 0$ corresponds to the second and fourth quadrants, while $\psi > 0$ to the first and third quadrants. Note that $\psi = 0$ represents a purely streamwise fluctuation. The quadrant analysis can be clearly expressed by the probability density function (PDF) of shear-stress angle, ψ. Figure 19(*b*) shows the PDF of ψ at the positions P_1, P_2 and P_3 marked in figure 18, corresponding to the nodal, saddle and middle plane. A strong orientation of the shear stress is related to the peak of N/N_T, where N/N_T represents the normalized number of samples. From figure 19(*b*), it is identified that the strong orientation is around -10.3° at P_1 and 7.3° at P_2, consistent with the wake-width shrinking and expanding in the near wake, while the strong orientation is around 0° at P_3, where the streamwise fluctuation is dominant.

The mean feature of the separated shear layer is investigated to understand the shear-layer growth with its evolution. Consequently, it is reasonable to use the vorticity thickness $\delta_\omega(x)$ and it can be expressed as (Simon *et al.* 2007)

$$\delta_\omega(x) = \frac{\Delta\tilde{U}}{(\partial\langle\tilde{u}(x,z)\rangle/\partial z)_{max}}, \tag{4.8}$$

where $\Delta\tilde{U}$ represents the resolved velocity difference magnitude across the shear layer. Figure 20(*a*) shows the evolution of δ_ω along the mean shear layers shed from the cylinders. For comparison, we first pay attention to the shear-layer growth from the

circular cylinder. The growth rate $\mathrm{d}\delta_\omega/\mathrm{d}x$ is around 0.25 in the region of $x/D < 0.5$ approximately, which is associated with the initial part of the shear layer just after separation and agrees well with the value for the compressible mixing layer past an axisymmetric trailing edge (Simon *et al.* 2007). Then, the growth rate $\mathrm{d}\delta_\omega/\mathrm{d}x$ increases quickly reaching a value equal to around 0.8 in the region of $0.5 < x/D < 1$ and becomes smaller on moving downstream. The large growth rate corresponding to high spreading rate leads to the existence of shock/wake interaction, as typically shown in figures 10(*d*) and 11(*d*), which results in high turbulence levels (Deck & Thorigny 2007; Xu *et al.* 2009*a*). Further, we analyse the shear-layer growth from the wavy cylinder. As shown in figure 20(*a*), the growth rates $\mathrm{d}\delta_\omega/\mathrm{d}x$ in the nodal, middle and saddle planes are nearly the same and are equal to around 0.15 in the region extending to $x/D = 2.5$ approximately. This growth rate even is less than the one at the initial region of the shear layer from the circular cylinder, indicating that instabilities of the free shear shed from the wavy cylinder develop quite slowly. It means that the 3D free shear layer from the wavy cylinder is more stable than that from the circular cylinder. Furthermore, the separated shear layer and its evolution are usually associated with transition mechanisms (e.g. Zdravkovich 1997; Mani, Moin & Wang 2009). As the growth rate of the shear layers shed from the wavy cylinder is relatively small, the effects of pre-separation transition on post-separation turbulence are weak. However, as moving shocks are formed over the circular cylinder, the shock/turbulence interaction plays a dominant role in the formation and evolution of the shear layer separated from the cylinder.

The shear-layer growth rate in this compressible flow is also affected by the compressibility effect, which can be reasonably well described by the convective Mach number, M_c (Bogdanoff 1983; Vreman *et al.* 1996; Freund *et al.* 2000; Pantano & Sarkar 2002). Usually, when $M_c < 0.6$, the instability process is mainly related to the bi-dimensional one with spanwise rolling eddies originating from the Kelvin–Helmholtz instability. When $0.6 < M_c < 1$, oblique modes are amplified and compete with bi-dimensional instability modes (e.g. Sandham, Yao & Lawal 2003; Simon *et al.* 2007). Following the estimation of M_c proposed by Simon *et al.* (2007), figure 20(*b*) shows the profiles of M_c along the mean shear layers. M_c varies smoothly and lies in the range of approximately 0.65–0.8 for the wavy cylinder, while M_c increases to around 0.9 and decreases quickly for the circular cylinder. According to the range of M_c, the instability processes for the separated shear-layer evolution are derived from the competition between the oblique modes and bi-dimensional instability modes.

To understand the instability development of the shear layer, turbulent fluctuations are further analysed. Figure 21 shows the profiles of the local peak Reynolds stresses $\{u_i'' u_j''\}/U_\infty^2$ (Herrin & Dutton 1997; Simon *et al.* 2007). For the shear-layer shed from the wavy cylinder, the values of the streamwise and transverse normal stresses and their shear stress remain small and increase very slowly, consistent with the low growth rate shown in figure 20(*a*). It means that the free shear layer is more stable. In contrast, the turbulent stresses or fluctuations are relatively large for the shear layer from the circular cylinder. Based on the analysis of the transport equations of Reynolds-stress components (not shown here), it is reasonably identified that the streamwise normal stress decreases and transfers to other components, resulting in the increase of the transverse normal stress and the shear stress in figure 21. Moreover, we have examined the production term in the transport equation of TKE and have noticed that the production term for the wavy cylinder is much less than the one for the circular cylinder. The turbulent stresses or fluctuations at the shear-layer

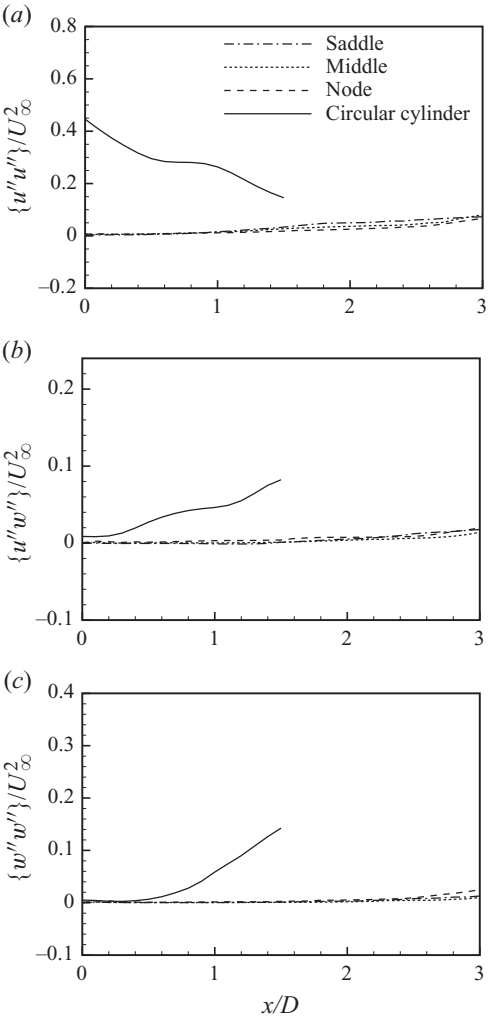

FIGURE 21. Evolution of the local-peak Reynolds stresses in the saddle, middle and nodal planes of the wavy cylinder and mid-spanwise plane of the circular cylinder: (*a*) streamwise normal stress $\{u''u''\}/U_\infty^2$, (*b*) streamwise-transverse shear stress $\{u''w''\}/U_\infty^2$ and (*c*) transverse normal stress $\{w''w''\}/U_\infty^2$.

shed from the wavy cylinder are significantly suppressed, leading to the more stable development of the free shear layer.

4.3.3. *Dynamics of the shear-layer evolution*

To reveal the dynamical processes of the shear-layers shed from the cylinders, we further discuss the behaviours of the Lamb vector divergence, which is associated with the momentum transport in the flow field (Wu *et al.* 2006). It is reasonable to use the Lamb vector divergence to describe the dynamical mechanisms by which adjacent high- and low-momentum fluid motions interact to effect a time rate of change of momentum (Hamman *et al.* 2008). The mechanisms related to the Lamb vector divergence play an important role in the evolution of the shear layer separated from the cylinder.

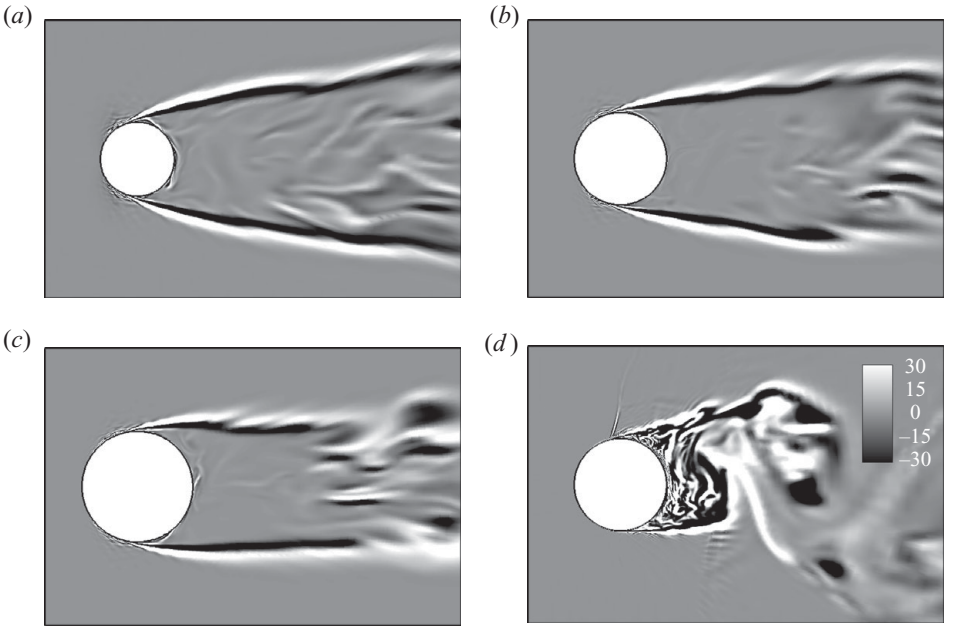

FIGURE 22. Distributions of the instantaneous Lamb vector divergence in the cross-section planes: (*a*) saddle, (*b*) middle, (*c*) nodal plane of wavy cylinder and (*d*) mid-spanwise plane of circular cylinder.

Figure 22 shows the instantaneous distributions of the Lamb vector divergence in the cross-section planes, corresponding to the instant in figures 10 and 11. For the wavy cylinder flow, two-layer structures with signs opposite to that of the Lamb vector divergence at the separated shear layer are observed. According to the analysis on the Lamb vector divergence (Hamman *et al.* 2008), both the negative and positive values represent vorticity bearing motions and straining motions, respectively. As a result, the dynamical processes in the two layers include that the interaction between the strong strain rate region and strong vorticity region may exchange momentum. The Lamb vector divergence reasonably well captures the temporal evolution of high- and low-momentum fluid flow, which is closely associated with the mechanisms that drive turbulent shear-layer evolution and lead to low turbulent fluctuations shown in figure 21. In addition, from the distributions of the Lamb vector divergence behind the circular cylinder, it is obviously identified that there exist complex structures and dynamical processes.

Based on theoretical analysis by Hamman *et al.* (2008), the distribution of the Lamb vector divergence is also related to the forces on a body. They investigated the flow around an oscillating circular cylinder for flow control and noticed that decreasing the area over which regions of positive and negative Lamb vector divergence interact leads to drag reduction. As shown in figure 22, the interaction area of positive and negative Lamb vector divergence mainly lies in the regions of shear-layers shed from the wavy cylinder. Compared with the area involving strong interaction behind the circular cylinder, it is qualitatively obtained that the interaction area behind the wavy cylinder is obviously decreased, resulting in the drag reduction in table 1.

The Lamb vector divergence appears as an acoustic source term in Lighthill's wave equation (Lighthill 1952; Howe 1975). Thus, the acoustic character is mainly

determined by turbulent shear-layer evolution near the cylinders in figure 22, consistent with the previous flow-noise prediction on turbulent boundary layers (Wang & Moin 2000; Wang, Freund & Lele 2006). Moreover, the distributions of the Lamb vector divergence apparently exhibit large magnitude behind the circular cylinder, compared with those behind the wavy cylinder. Therefore, it is reasonable to predict that the wavy cylinder may also play an effective role in acoustic control by suppressing the acoustic source term in Lighthill's wave equation.

5. Concluding remarks

Numerical investigation of the compressible flow past a wavy cylinder was carried out by means of an LES technique for a free-stream Mach number $M_\infty = 0.75$ and a Reynolds number based on the mean diameter $Re = 2 \times 10^5$. For comparison, the compressible flow past a corresponding circular cylinder was also calculated. Various fundamental mechanisms dictating the intricate flow phenomena, including drag reduction and fluctuating force suppression, shock waves and shocklets elimination, 3D separation and separated shear-layer instability, and flow-field structures, were examined systematically and are summarized briefly as follows.

The behaviour of the forces exerted on the cylinder is an important issue associated with the control of flow over a bluff body. As a result, the mean drag coefficient of the wavy cylinder is less than that of a corresponding circular cylinder with a drag reduction up to 26 %. Based on the analysis of drag decomposition, we have identified that the drag reduction due to the shearing process prevails over that due to the compressing process in this flow. The fluctuating lift coefficient is greatly suppressed to be nearly zero. As the Reynolds number considered is $O(10^5)$, the pressure force plays a dominant role in the total forces on the cylinder. We have found that a higher base pressure of the wavy cylinder is mainly responsible for the drag reduction. Moreover, the pressure fluctuation on the wavy cylinder is significantly suppressed in the base region, resulting in the fluctuating force reduction.

For the compressible flow past the cylinders, the shearing and compressing processes should be coupled to affect the overall flow characteristics and are related to the mechanisms of the flow control. The BVF represents an on-surface dynamic process which causes the formation of vortical structures, and is in turn dominated by the tangent pressure gradient which measures the local dynamics of the compressing process. The BVF on the cylinders occurs obviously in the attached flow region and drops quickly at flow separation. It is found that the positive BVF peak on the wavy cylinder at the middle position is attenuated clearly, compared with that on the circular cylinder, because of the suppression of shock formation for the wavy cylinder flow. Moreover, the vortical structures in the near wake are closely associated with the dynamics on a body and flow control over a bluff body. Some prominent differences of the vortical structures behind the wavy and circular cylinders are identified. The vortical structures near the base region of the wavy cylinder are significantly less vigorous than those of the circular cylinder. The 3D shear-layer shed from the wavy cylinder is more stable than that from the circular cylinder. The vortex roll up of the shear layer separated from the wavy cylinder is delayed to a further downstream position, leading to a reduction of the suction near the base of the cylinder or a higher-base-pressure distribution.

To assess the passive control of the compressible flow past a wavy cylinder, some intricate phenomena relevant to the compressible effect, such as moving shock waves, LSZs and shocklets and shock/turbulence interaction, have been studied. For the

circular cylinder flow, the moving shock waves are formed over the cylinder and in the near wake, resulting in complex shock/boundary layer and shock/wake interaction, consistent with the experimental observations (Rodriguez 1984; Thombi *et al.* 2002). Meanwhile, the existence of shocklets accompanied by the stronger LSZ is detected in the near wake and can induce the high level of turbulent fluctuations. The extracted shocklets are shown to exhibit basically a curved dish-like structure for the first time. In contrast, the shocks and shocklets are not detected for the wavy cylinder flow. As a result, the shock-induced pressure drag is avoided. The elimination of shock waves and shocklets around the wavy cylinder plays an important role in the compressible flow control and results in a significant suppression of the turbulent fluctuations behind the wavy cylinder which is related to the lower fluctuating surface pressure (Nakamura & Igarashi 2008). In addition, the wavy surface may provide an effective way of shock control, say an airfoil with small amplitude wavy surface for transonic buffet control.

Characteristics of the 3D separation and shear-layer evolution are investigated to understand the mechanisms of flow control. As the 3D separation depends on the local dynamics, it is found that the spanwise pressure gradient and the baroclinic term in the transport equation of vorticity play an important role in generating the oblique vortical perturbation to the separated shear layer, which may moderate the increase of the amplitude of fluctuation of the shear layer (Prasad & Williamson 1997) and is of help in its more stable development. Further, based on the analysis of the convective Mach number, it is identified that the instability processes in the separated shear-layer evolution are derived from the competition between the oblique modes and bi-dimensional instability modes. Compared with the circular cylinder flow, the shear-layer growth rate in the wavy cylinder flow becomes smaller and the turbulent fluctuation becomes weaker. Moreover, the dynamical processes of the flow evolution are discussed in terms of the instantaneous Lamb vector divergence. The Lamb vector divergence reasonably well captures the temporal evolution of high- and low-momentum fluid flow with two-layer structures in the separated shear layer. Because of the passive control of the compressible flow past a wavy cylinder, the Lamb vector divergence becomes weakened, which can reasonably be associated with the drag reduction and the suppression of the acoustic source term in Lighthill's wave equation for acoustic control.

The authors are very grateful to Professor J.-Z. Wu for the valuable discussions. This work was supported by the National Natural Science Foundation of China (Grant Nos. 11072236 and 10832010) and the Knowledge Innovation Foundation of the Chinese Academy of Sciences (Grant No. KJCX2-YW-L05).

REFERENCES

Adrian, R. J. & Moin, P. 1988 Stochastic estimation of organized turbulent structure: homogeneous shear flow. *J. Fluid Mech.* **190**, 531–559.

Ahmed, A. & Bays-Muchmore, B. 1992 Transverse flow over a wavy cylinder. *Phys. Fluids* A **4**, 1959–1967.

Ahmed, A., Khan, M. J. & Bays-Muchmore, B. 1993 Experimental investigation of a three-dimensional bluff-body wake. *AIAA J.* **31**, 559–563.

Anderson, E. & Szewczyk, A. 1997 Effects of a splitter plate on the near wake of a circular cylinder in 2 and 3-dimensional flow configurations. *Exp. Fluids* **23**, 161–174.

Arcas, D. & Redekopp, L. 2004 Aspects of wake vortex control through base blowing/suction. *Phys. Fluids* **16**, 452–456.

Barre, S., Quine, C. & Dussauge, J. P. 1994 Compressibility effects on the structure of supersonic mixing layers: experimental results. *J. Fluid Mech.* **259**, 47–78.

Batham, J. P. 1973 Pressure distributions on circular cylinders at critical Reynolds numbers. *J. Fluid Mech.* **57**, 209–228.

Berkooz, G., Holmes, P. & Lumley, J. L. 1993 The proper orthogonal decomposition in the analysis of turbulent flows. *Annu. Rev. Fluid Mech.* **25**, 539–575.

Bogdanoff, D. W. 1983 Compressibility effects in turbulent shear layer. *AIAA J.* **21**, 926–927.

Bushnell, D. A. 2004 Shock wave drag reduction. *Annu. Rev. Fluid Mech.* **36**, 81–96.

Cai, J., Chng, T. L. & Tsai, H. M. 2008 On vortical flows shedding from a bluff body with a wavy trailing edge. *Phys. Fluids* **20**, 064102.

Chakraborty, P., Balachandar, S. & Adrian, R. J. 2005 On the relationships between local vortex identification schemes. *J. Fluid Mech.* **535**, 189–214.

Chang, C.-C. & Lei, S.-Y. 1996 On the sources of aerodynamic forces: steady flow around a cylinder or a sphere. *Proc. R. Soc. Lond.* A **452**, 2369–2395.

Chen, L.-W., Xu, C.-Y. & Lu, X.-Y. 2010*a* Numerical investigation of the compressible flow past an aerofoil. *J. Fluid Mech.* **643**, 97–126.

Chen, L.-W., Xu, C.-Y. & Lu, X.-Y. 2010*b* Large-eddy simulation of opposing-jet-perturbed supersonic flow past a hemispherical nose. *Mod. Phys. Lett.* B **24**, 1287–1290.

Choi, H., Jeon, W.-P. & Kim, J. 2008 Control of flow over a bluff body. *Annu. Rev. Fluid Mech.* **40**, 113–139.

Chorin, A. J. 1994 *Vorticity and Turbulence*. Springer.

Clemens, N. T. & Mungal, M. G. 1995 Large-scale structure and entrainment in the supersonic mixing layer. *J. Fluid Mech.* **284**, 171–216.

Deck, S. & Thorigny, P. 2007 Unsteadiness of an axisymmetric separating-reattaching flow. *Phys. Fluids* **19**, 065103.

Delaunay, Y. & Kaiktsis, L. 2001 Control of circular cylinder wakes using base mass transpiration. *Phys. Fluids* **13**, 3285–3302.

Desjardin, P. E. & Frankel, S. H. 1998 Large-eddy simulation of a non-premixed reacting jet: application and assessment of subgrid-scale combustion models. *Phys. Fluids* **10**, 2298–2314.

Ducros, F., Ferrand, V., Nicoud, F., Weber, C., Darracq, D., Gacherieu, C. & Poinsot, T. 1999 Large-eddy simulation of the shock/turbulence interaction. *J. Comput. Phys.* **152**, 517–549.

Freund, J. B., Lele, S. K. & Moin, P. 2000 Compressibility effects in a turbulent annular mixing layer. Part 1. Turbulence and growth rate. *J. Fluid Mech.* **421**, 229–267.

Fureby, C. 1996 On subgrid-scale modelling in large eddy simulations of compressible fluid flow. *Phys. Fluids* **8**, 1301–1311.

Garnier, E., Sagaut, P. & Deville, M. 2002 Large eddy simulation of shock/homogeneous turbulence interaction. *Comput. Fluids* **31**, 245–268.

Germano, M., Piomelli, U., Moin, P. & Cabot, W. H. 1991 A dynamic subgrid-scale eddy viscosity model. *Phys. Fluids* A **3**, 1760–1765.

Gruber, M. R., Messersmith, N. L. & Dutton, J. G. 1993 Three-dimensional velocity field in a compressible mixing layer. *AIAA J.* **31**, 2061–2067.

Hafez, M. & Wahba, E. 2007 Simulations of viscous transonic flows over lifting airfoils and wings. *Comput. Fluids* **36**, 39–52.

Hamman, C. W., Klewicki, J. C. & Kirby, R. M. 2008 On the Lamb vector divergence in Navier–Stokes flows. *J. Fluid Mech.* **610**, 261–284.

Herrin, J. L. & Dutton, J. C. 1995 Effect of a rapid expansion on the development of compressible free shear layers. *Phys. Fluids* **7**, 159–171.

Herrin, J. L. & Dutton, J. C. 1997 The turbulence structure of a reattaching axisymmetric compressible free shear layers. *Phys. Fluids* **9**, 3502–3512.

Hill, D. J., Pantano, C. & Pullin, D. I. 2006 Large-eddy simulation and multiscale modelling of a Richtmyer–Meshkov instability with reshock. *J. Fluid Mech.* **557**, 29–61.

Howe, M. S. 1975 Contributions to the theory of aerodynamic sound, with application to excess jet noise and the theory of the flute. *J. Fluid Mech.* **71**, 625–673.

Hwang, J. Y., Yang, K. S. & Sun, S. H. 2003 Reduction of flow-induced forces on a circular cylinder using a detached splitter plate. *Phys. Fluids* **15**, 2433–2436.

Jeong, J. & Hussain, F. 1995 On the identification of a vortex. *J. Fluid Mech.* **285**, 69–94.

Kawai, S. & Fujii, K. 2005 Computational study of supersonic base flow using hybrid turbulence methodology. *AIAA J.* **43**, 1265–1275.

Knight, D., Zhou, G., Okong'o, N. & Shukla, V. 1998 Compressible large eddy simulation using unstructured grids. *AIAA Paper* 1998-0535.

Lam, K. & Lin, Y. F. 2008 Large eddy simulation of flow around wavy cylinders at a subcritical Reynolds number. *Intl J. Heat Fluid Flow* **29**, 1071–1088.

Lam, K. & Lin, Y. F. 2009 Effects of wavelength and amplitude of a wavy cylinder in cross-flow at low Reynolds numbers. *J. Fluid Mech.* **620**, 195–220.

Lam, K., Wang, F. H., Li, J. Y. & So, R. M. C. 2004*a* Experimental investigation of the mean and fluctuating forces of wavy (varicose) cylinders in a cross-flow. *J. Fluids Struct.* **19**, 321–334.

Lam, K., Wang, F. H. & So, R. M. C. 2004*b* Three-dimensional nature of vortices in the near wake of a wavy cylinder. *J. Fluids Struct.* **19**, 815–833.

Lee, S., Lele, S. K. & Moin, P. 1991 Eddy shocklets in decaying compressible turbulence. *Phys. Fluids* A **3**, 657–664.

Lee, S. J. & Nguyen, A. T. 2007 Experimental investigation on wake behind a wavy cylinder having sinusoidal cross-sectional area variation. *Fluid Dyn. Res.* **39**, 292–304.

Lighthill, M. J. 1952 On sound generated aerodynamically. Part I. *Proc. R. Soc. Lond.* A **211**, 564–587.

Lighthill, M. J. 1963 Introduction of boundary layer theory. In *Laminar Boundary Layers*, (ed. L. Rosenhead), pp. 46–113, Oxford University Press.

Lilly, D. K. 1992 A proposed modification of the Germano subgrid-scale closure method. *Phys. Fluids* **4**, 633–635.

Loginov, M. S., Adams, N. A. & Zheltovodov, A. A. 2006 Large-eddy simulation of shock-wave/turbulent-boundary-layer interaction. *J. Fluid Mech.* **565**, 135–169.

Lu, X.-Y., Wang, S. W., Sung, H. G., Hsieh, S. Y. & Yang, V. 2005 Large eddy simulations of turbulent swirling flows injected into a dump chamber. *J. Fluid Mech.* **527**, 171–195.

Lu, S. S. & Willmarth, W. W. 1973 Measurements of the structure of the Reynolds stress in a turbulent boundary layer. *J. Fluid Mech.* **60**, 481–551.

Lumley, J. L. 1967 Rational approach to relations between motions of differing scales in turbulent flows. *Phys. Fluids* **10**, 1405–1408.

Macha, J. M. 1977 Drag of circular cylinders at transonic Mach numbers. *J. Aircraft* **14**, 605–607.

Mani, A., Moin, P. & Wang, M. 2009 Computational study of optical distortions by separated shear layers and turbulent wakes. *J. Fluid Mech.* **625**, 273–298.

Martin, M. P., Piomelli, U. & Candler, G. V. 1999 Subgrid-scale models for compressible large-eddy simulations. *Theor. Comput. Fluid Dyn.* **13**, 361–376.

Miserda, R. F. B. & Leal, R. G. 2006 Numerical simulation of the unsteady aerodynamic forces over a circular cylinder in transonic flow. *AIAA Paper* 2006–1408.

Moin, P., Squires, K., Cabot, W. & Lee, S. 1991 A dynamic subgrid-scale model for compressible turbulence and scalar transport. *Phys. Fluids* A **3**, 2746–2757.

Murthy, V. S. & Rose, W. C. 1978 Detailed measurements on a circular cylinder in cross flow. *AIAA J.* **16**, 549–550.

Nakamura, H. & Igarashi, T. 2008 Omnidirectional reductions in drag and fluctuating forces for a circular cylinder by attaching rings. *J. Wind Engng Ind. Aerodyn.* **96**, 887–899.

Oertel, H. & Affiliation, J. 1990 Wakes behind blunt bodies. *Annu. Rev. Fluid Mech.* **22**, 539–564.

Owen, J. C. & Bearman, P. W. 2001 Passive control of viv with drag reduction. *J. Fluids Struct.* **15**, 597–605.

Ozono, S. 1999 Flow control of vortex shedding by a short splitter plate asymmetrically arranged downstream of a cylinder. *Phys. Fluids* **11**, 2928–2934.

Pantano, C. & Sarkar, S. 2002 A study of compressibility effects in the high-speed turbulent shear layer using direct simulation. *J. Fluid Mech.* **451**, 329–371.

Papamoschou, D. & Roshko, A. 1988 The compressible turbulent shear layer: an experimental study. *J. Fluid Mech.* **197**, 453–477.

Peake, N. & Crighton, D. G. 2000 Active control of sound. *Annu. Rev. Fluid Mech.* **32**, 137–164.

Piomelli, U. 1999 Large-eddy simulation: achievements and challenges. *Prog. Aerosp. Sci.* **35**, 335–362.

Pirozzoli, S., Grasso, F. & Gatski, T. B. 2004 Direct numerical simulation and analysis of a spatially evolving supersonic turbulent boundary layer at $M = 2.25$. *Phys. Fluids* **16**, 530–545.

Pope, S. B. 2000 *Turbulent Flows*. Cambridge University Press.

Prasad, A. & Williamson, C. H. K. 1997 The instability of the shear layer separating from a bluff body. *J. Fluid Mech.* **333**, 375–402.

Robinson, S. K. 1991 Coherent motions in the turbulent boundary layers. *Annu. Rev. Fluid Mech.* **23**, 601–639.

Rodriguez, O. 1984 The circular cylinder in subsonic and transonic flow. *AIAA J.* **22**, 1713–1718.

Salvetti, M. V. & Banerjee, S. 1995 A priori test of a new dynamic subgrid-scale model for finite difference large-eddy simulations. *Phys. Fluids* **7**, 2831–2847.

Samtaney, R., Pulin, D. I. & Kosović, B. 2001 Direct numerical simulation of decaying compressbilce turbulence and shocklet statistics. *Phys. Fluids* **13**, 1415–1430.

Sandham, N. D. & Reynolds, W. C. 1991 Three-dimensional simulations of large eddies in the compressible mixing layer. *J. Fluid Mech.* **224**, 133–158.

Sandham, N. D., Yao, Y. F. & Lawal, A. A. 2003 Large-eddy simulation of transonic turbulent flow over a bump. *Intl J. Heat Fluid Flow* **24**, 584–595.

Sarkar, S. 1995 The stabilizing effect of compressibility in turbulent shear flow. *J. Fluid Mech.* **282**, 163–186.

Shvets, A. I. 1983 Pressure fluctuations during flow around blunt bodies. *J. Appl. Mech. Tech. Phys.* **24**, 193–199.

Simon, F., Deck, S., Guillen, P., Sagaut, P. & Merlen, A. 2007 Numerical simulation of the compressible mixing layer past an axisymmetric trailing edge. *J. Fluid Mech.* **591**, 215–253.

Smagorinsky, J. 1963 General circulation experiments with the privative equations. Part I. The basic experiment. *Mon. Weath. Rev.* **91**, 99–164.

Stanewsky, E. 2001 Adaptive wing and flow control technology. *Prog. Aerosp. Sci.* **37**, 583–667.

Thomas, J. L. & Salas, M. D. 1986 Far-field boundary conditions for transonic lifting solutions to the Euler equations. *AIAA J.* **24**, 1074–1080.

Thombazis, N. & Bearman, P. W. 1997 A study of three-dimensional aspects of vortex shedding from a bluff body with a mild geometric disturbance. *J. Fluid Mech.* **330**, 85–112.

Thombi, L., Daisuke, H. & Yoshiaki, N. 2002 Passive separation control on a body at transonic speed. *Trans. Japan Soc. Aerosp. Space Sci.* **44**, 229–237.

Truesdell, C. 1954 *The Kinematics of Vorticity*. Indiana University Press.

Vreman, B., Kuerten, H. & Geurts, B. 1995 Shocks in direct numerical simulation of the confined three-dimensioal mixing layer. *Phys. Fluids* **7**, 2105–2107.

Vreman, A. W., Sandham, N. D. & Luo, K. H. 1996 Compressible mixing layer growth rate and turbulence characteristics. *J. Fluid Mech.* **320**, 235–258.

Wallace, J. M., Eckelmann, H. & Brodkey, R. S. 1972 The wall region in turbulent shear flow. *J. Fluid Mech.* **54**, 39–48.

Wang, M., Freund, J. B. & Lele, S. K. 2006 Computational prediction of flow-generated sound. *Annu. Rev. Fluid Mech.* **38**, 483–512.

Wang, M. & Moin, P. 2000 Computation of trailing-edge flow and noise using large-eddy simulation. *AIAA J.* **38**, 2201–2209.

Wang, S. W., Yang, V., Hsiao, G., Hsieh, S. Y. & Mongia, H. C. 2007 Large-eddy simulations of gas-turbine swirl injector flow dynamics. *J. Fluid Mech.* **583**, 99–122.

Williamson, C. H. K. & Govardhan, R. 2004 Vortex-induced vibrations. *Annu. Rev. Fluid Mech.* **36**, 413–455.

Willmarth, W. W. & Lu, S. S. 1972 Structure of the Reynolds stress near the wall. *J. Fluid Mech.* **55**, 65–92.

Wu, J.-Z., Lu, X.-Y. & Zhuang, L.-X. 2007 Integral force acting on a body due to local flow structures. *J. Fluid Mech.* **576**, 265–286.

Wu, J.-Z., Ma, H.-Y. & Zhou, M.-D. 2006 *Vorticity and Vortex Dynamics*. Springer.

Xu, C.-Y., Chen, L.-W. & Lu, X.-Y. 2009*a* Effect of Mach number on transonic flow past a circular cylinder. *Chin. Sci. Bull.* **54**, 1886–1893.

Xu, C.-Y., Chen, L.-W. & Lu, X.-Y. 2009*b* Numerical simulation of shock wave and turbulence interaction over a circular cylinder. *Mod. Phys. Lett. B* **23**, 233–236.

Yao, Y. F. & Sandham, N. D. 2002 Direct numerical simulation of turbulent trailing-edge flow with base flow control. *AIAA J.* **40**, 1708–1716.

Yoshizawa, A. 1986 Statistical theory for compressible turbulent shear flows, with the application to subgrid modeling. *Phys. Fluids* **29**, 2152–2164.

Zdravkovich, M. M. 1997 *Flow Around Circular Cylinders*. Oxford University Press.

Zhang, W., Dai, C. & Lee, S. J. 2005 PIV measurements of the near-wake behind a sinusoidal cylinder. *Exp. Fluids* **38**, 824–832.